SUPPORTING INFORMATION

Breaking the Nanoparticle Loading/Dispersion Dichotomy in Polymer Nanocomposites with the Art of Croissant-Making

*Giovanni Santagiuliana[a], Olivier T. Picot[a,b], Maria Crespo[a], Harshit Porwal[a,b], Han Zhang[a,b], Yan Li[a,c], Luca Rubini[d], Samuele Colonna[e], Alberto Fina[e], Ettore Barbieri[a,f], Anne B. Spoelstra[g], Giulia Mirabello[g], Joseph P. Patterson[g], Lorenzo Botto[a], Nicola M. Pugno[d,h,a], Ton Peijs[a,b], Emiliano Bilotti[a,b] **

[a] School of Engineering and Materials Science, Queen Mary University of London, Mile End Road, London E1 4NS, U.K.

[b] Nanoforce Technology Limited, Mile End Road, London E1 4NS, U.K.

[c] Gemmological Institute, China University of Geosciences, 388 Lumo Rd., Wuhan, China 430074.

[d] Laboratory of Bio-inspired & Graphene Nanomechanics, Department of Civil, Environmental and Mechanical Engineering, University of Trento, Via Mesiano 77, 38123 Trento, Italy.

[e] Dipartimento di Scienza Applicata e Tecnologia, Politecnico di Torino, 15121 Alessandria, Italy.

[f] Japan Agency for Marine-Earth Science and Technology, Department of Mathematical Science and Advanced Technology, Yokohama Institute for Earth Sciences, 3173-25, Showa-machi, Kanazawa-ku, Yokohama-city, Kanagawa, 236-0001, Japan.

[g] Laboratory of Materials and Interface Chemistry & Centre for Multiscale Electron Microscopy
Department of Chemical Engineering and Chemistry, Eindhoven University of Technology, Eindhoven,
The Netherlands.

[h] Ket-Lab, Edoardo Amaldi Foundation, Italian Space Agency, Via del Politecnico, 00133 Rome, Italy.

Corresponding Author

* E-mail address: e.bilotti@qmul.ac.uk

Contents

S.1 Characterization techniques

The **lateral size** of the GNP powder particles was characterized by scanning electron microscopy (SEM, FEI Inspect-F). One hundred particles were measured for statistical determination of the particles' length and width. The length was considered as the longest side, whereas the width was measured along the normal of the length.

The **thickness** of GNP powder particles was characterized by atomic force microscopy (AFM, NT-MDT Ntegra) in semi-contact mode. The thickness of a particle was calculated by averaging the height profile. Twenty particles were measured for statistical determination of particles' thickness.

X-ray diffraction (XRD) studies were carried out at room temperature on a Panalytical X'Pert Pro diffractometer in reflection mode between 5°-70° 2θ and 2.5°-35° Ω, moving the samples with a spinner revolution time of 4 s. The X-ray tube used a tension of 45 kV, and 40mA of current. The incident beam employed the k-alpha1 radiation (0.154 nm) of the cupper anode. A filter made of nickel selected the diffracted beam. The crystalline interlayer spacing of GNP was determined by using Bragg's law:

$$d = \frac{\lambda}{2\sin(\theta)}$$

Equation S1.

where λ is the incident wavelength, and ϑ is the Bragg's angle of the (002) reflection around 26.6° 2θ. The mean thickness of GNP, and the mean sizes of the LLDPE crystallites were calculated with the Debye-Scherrer's formula:[1,2]

$$T = \frac{0.9\,\lambda}{\beta\cos(\theta)}$$

Equation S2.

where β is the full-width at half-maximum (FWHM) in radians of graphite (002) peak, or LLDPE (110) and (200) peaks around 21.6° 2θ and 23.8° 2θ, obtained from a single Gaussian peak fit between 20°-35° 2θ for GNP powder, and from a multiple Gaussian peaks fit between 10°-35° 2θ for pure LLDPE and nanocomposites samples.

The degree of LLDPE crystallinity (X_c) was calculated from the integrated intensities of the (110) and (200) peaks, and from the area of the amorphous halo on which the crystalline peaks are superimposed, as described by the Hermans-Weidinger method:[2,3]

$$X_c = \frac{I_c^{110} + I_c^{200}}{I_a + I_c^{110} + I_c^{200}} \cdot 100$$

Equation S3.

The **microstructures** of the nanocomposites were studied by analysing the cross-sections of cryogenically broken samples by scanning electron microscopy (SEM, FEI Inspect-F). The specimens were previously gold-sputtered to cover them with a conductive film 6-8 nm thick. For statistical determination of filler agglomerates contained in nanocomposites of LLDPE + 4.8 vol.% GNP as a function of P&F cycles, diameter (the longest side) and thickness (segment along the normal of diameter) of each filler agglomerate was measured from at least three different specimen for each P&F sample, in order to have at least 100 measured agglomerates per sample. The aspect-ratio of each agglomerate was calculated by dividing its diameter by its thickness. The histograms of agglomerates' diameter, thickness, and aspect-ratio were fitted with a log-normal function in order to find out the geometrical mean values as a function of P&F cycles.

Electrical conductivity measurements were performed in-plane and out-of-plane of the samples by a 2-points probe connected to a DC system power supply (Agilent 6614c, 0-100V/0-0.5A), and a picoammeter (Keithely 6485, 2nA–20mA). A low electric field from 0 to 1.5 V/mm was applied in both cases in order to avoid a non-linear current-voltage relationship,[4] and 20 voltage-current data points were measured and recorded after waiting 100 ms at each 0.075 V/mm interval. Five specimens per sample were tested both for in-plane and out-of-plane measurements. Length (L), width (W), and thickness (*T*) of each specimen were measured and recorded before testing (in particular, specimen 15×8×0.3 mm^3 of nominal size were used for in-plane, and 10×10×0.3 mm^3 for out-of-plane measurements). The electrical conductivity of each specimen, σ, was calculated after a linear fit of the current-voltage data:

$$\sigma = \frac{BL}{WT}$$

Equation S4.

where *B* is the slope of the fitting equation ($y = A + Bx$, with *y* = current, and *x* = voltage).

Tensile tests were executed following the ASTM D 638-02a standard method with specimen type V, performing five specimens per sample in a universal testing machine (Instron 5566), equipped with a 1 kN load cell. The experimental data points were collected every 10 ms. Width and thickness of each specimen were measured before testing. LLDPE samples were tested at 1 mm/min until a strain of 10% was reached, then the tests continued at 30 mm/min until failure. Nanocomposites and a reference sample of pure LLDPE were tested at 1 mm/min until breakage. The stress-strain curves were reconstructed using the collected load-extension data points and the specimens' sizes. The elastic modulus of each specimen was determined from the slope of a linear fit of the stress-strain curve executed over a strain range of 0.25% after the Toe's region. The yield point was considered as the first zero-slope point on the stress-strain curve.

Thermal diffusivity measurements were carried out using an incident lase pulse on the sample and recording temperature signal versus time with an IR detector. The thermal conductivity of the samples were calculated by multiplying the recorded thermal diffusivity with the samples' density and heat capacity (the latter was estimated by rule of mixture using a heat capacity of 1.555 J g^{-1} K^{-1} for LLDPE, and one of 0.709 J g^{-1} K^{-1} for GNP).

Joule/Self heating experiments were performed by applying a voltage using an AC power source from 0 to 240 V in steps. Current was recorded using a Tenma 72-7765 digital multimeter. Change in temperature on the sample surface was recorded with time by applying thermocouples to at least 3 different points. Thermal images of the samples were taken using a FLIR E40 thermal camera. The samples were placed in between insulating glass fibre mats to avoid heat loss.

Strain-sensing tests were performed using samples with nominal size of $50 \times 0.3 \times 15$ mm^3 in a universal testing machine (Instron 5566), equipped with a 1 kN load cell. The grips were 20 mm far from each other at the beginning of each test. The extremities of the samples were previously coated with silver paint in order to assure a good electrical contact with a 2-points probe setup connected to a DC system power supply (Agilent 6614c, 0-100V/0-0.5A), and a picoammeter (Keithely 6485, 2nA–20mA). Two types of strain-sensing tests were conducted: cyclic tests consisting of stretching the samples between 0.5 and 3% of nominal strain for five times at a speed of 1 mm/min, and recording the resistance every second; and tensile tests at a speed of 1 mm/min until failure, recording the resistance every second.

Electrochemical impedance spectroscopy (EIS) measurements were performed between 100 mHz and 1 MHz using a SP-300 (SN 0623) Bio-Logic impedance analyser controlled by the EC-lab software. An AC-potential perturbation of 100 mV was used for all experiments. Nanocomposite films of ~300 µm in thickness were cut with a 1 cm diameter hole puncher. Round samples were placed between two full metallic electrodes that were tightened together with a screw press (*aka.* supercapacitor energy storage module). The permittivity of composites was determined from the impedance data according to:[5] $\varepsilon' \approx Z''/(Z''^2 + Z''^2)$ and $\varepsilon'' \approx Z'/(Z''^2 + Z''^2)$. As the shape factor (thickness/area) of all samples is equivalent, permittivity magnitudes were compared excluding this value.

Differential scanning calorimetry (DSC) analysis were performed on a TA Instruments DSC25 following this procedure:

- 1st DSC cycle: ramp 10 °C/min to -20.000 °C; isothermal 5.0 min; ramp 10 °C/min to 160.000 °C; isothermal 5.0 min; ramp 10 °C/min to -20.000 °C; isothermal 5.0 min;
- 2nd DSC cycle: ramp 10 °C/min to 160.000 °C; ramp 10 °C/min to -20.000 °C.

S.2 X-ray diffraction (XRD) observations

Figure S1 shows the XRD patterns of GNP powder, neat linear low density polyethylene (LLDPE) at different pressing and folding (P&F) cycles, nanocomposites of LLDPE + 0.21 vol.% of graphite nanoplatelets (GNP) at different P&F cycles, nanocomposites of LLDPE + 4.8 vol.% of GNP at different P&F cycles, and a nanocomposite of LLDPE + 35 vol.% of GNP at 200 P&F cycles. All the details of these XRD patterns are presented in Table S1.

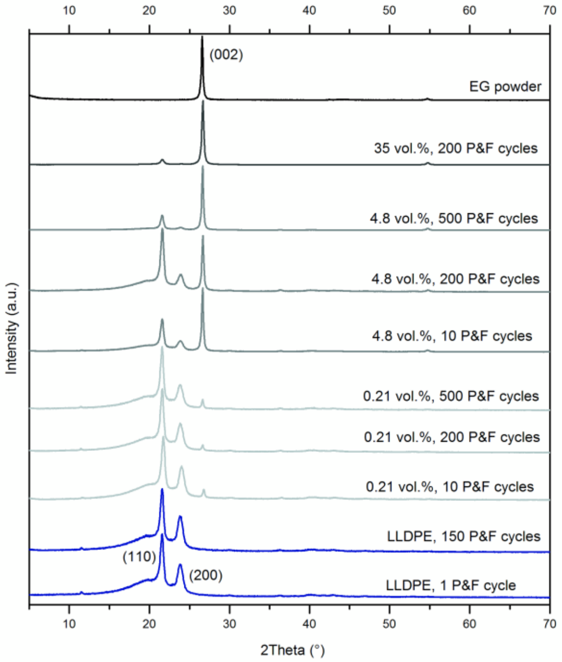

Figure S1. XRD patterns of GNP powder, neat LLDPE, and LLDPE nanocomposites containing specified GNP loadings.

Table S1. Values found or calculated from all the XRD patterns of Figure S1.

Sample	P&F cycles	GNP (002) peak (° 2θ)	$\bar{t}$ of GNP (nm)	LLDPE crystallite size from (110) peak (nm)	LLDPE crystallite size from (200) peak (nm)	LLDPE crystallinity, X_c (%)
GNP powder		26.57	27			
LLDPE	1			16.6	11.1	32.4 ± 0.6
	150			16.9	11.2	33.4 ± 0.4
LLDPE + 0.21 vol.% GNP	10	26.77	26	16.5	11.1	32.5 ± 0.4
	200	26.63	33	17.3	11.1	31.5 ± 0.4
	500	26.63	31	17.3	11.0	33.1 ± 0.5
LLDPE + 4.8 vol.% GNP	10	26.62	28	17.4	11.6	34.0 ± 0.6
	200	26.66	26	17.5	11.3	36.6 ± 0.6
	500	26.63	28	18.1	12.5	36.7 ± 1.3
LLDPE + 35 vol.% GNP	200	26.66	27	15.0	11.0	40 ± 4

S.3 Nanofiller characterization

Figure S2 shows the SEM and AFM observations of the as received GNP powder. The particles appeared to be irregularly shaped (see Figure S2a), probably resulting from the aggregation of smaller sub-particles, as suggested by the observation in Figure S2b.

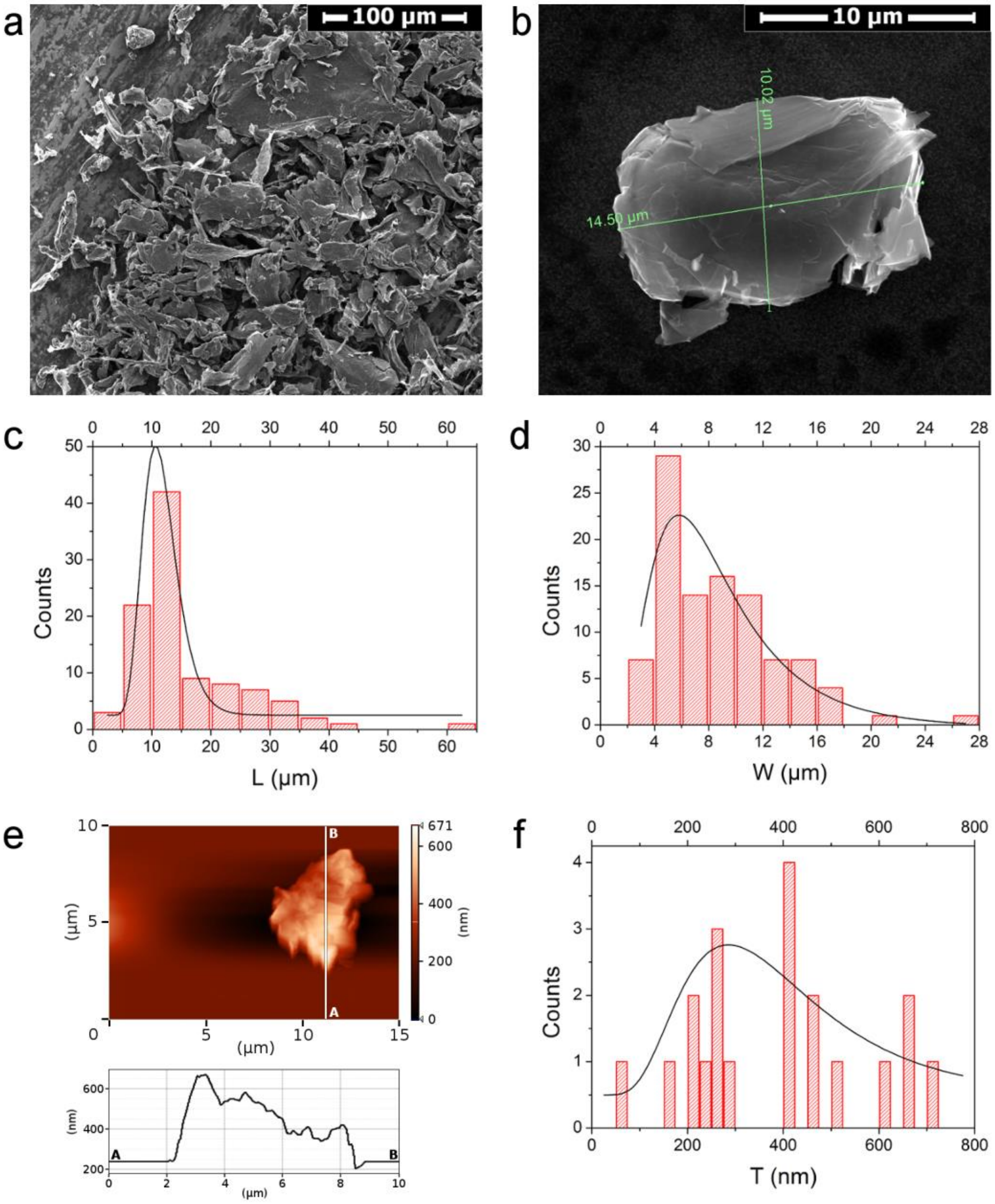

*Figure S2. SEM images of GNP powder (**a**-**b**); size distributions of the longest and shortest sides obtained from SEM measurements of 100 GNP powder particles (**c**-**d**); AFM image of an GNP powder particle with the thickness profile of the highlighted AB line (**e**); and thickness distribution obtained from AFM measurements of 20 GNP powder particles (**f**).*

Parts c and d of Figure S2 show the size distributions of the longest (L) and shortest (W) sides of 100 GNP powder particles. These distributions were fitted with a log-normal function,[6] obtaining the following geometric mean values (that is, the median of each distribution) and geometric standard deviations (GSD): $\overline{L}$ = 11.4 µm with GSD_L = 1.3, and $\overline{W}$ = 7.8 µm with GSD_W = 1.7. Note that the geometric coefficient of variation is 30% for L, and 72% for W, meaning that the distribution of the shortest particle side is more broadened. Since most of the measured particles (63%) have a W/L ratio greater than 0.5, the GNP powder particles can be approximated to disc-like particles with a mean diameter $\overline{D} = \sqrt{\overline{LW}}$ = 9.4 µm.

The thickness distribution of the GNP powder particles is shown in Figure S2f, and was fitted with a log-normal function, obtaining the following values: $\overline{T}$ = 364 nm, GSD_T = 1.6. The geometric coefficient of variation of T is high: 64%, mainly because of the low number of measurements (20), and the irregular thickness of each particle (see the thickness profile of the particle in Figure S2e), probably due to some folded sides, or different numbers of agglomerated sub-particles, as suggested before.

The density of these GNP powder particles cannot be measured, so the volume fractions occupied by these GNP powder particles inside the nanocomposites cannot be calculated. However, the density of pure graphite, d_G = 2.2 g/cm^3,[7] can be attributed approximatively. In this way, by using d_G and the above-mentioned values of $\overline{D}$ and $\overline{T}$, it is possible to calculate a specific surface area of $\frac{\pi\overline{D}^2/2+\pi\overline{D}\overline{T}}{d_G\pi\overline{D}^2\overline{T}/4} = 2.7$ m^2/g for GNP, which is much lower than the reported BET surface area (25 m^2/g). This confirms the initial hypothesis that the observed GNP powder particles are made of agglomerated sub-particles (for example graphite nanoplatelets, GNP).

The density and thickness of these sub-particles can be deduced from the XRD pattern of GNP powder (Figure S1).[8] The graphite (002) peak centred on 26.6° 2θ (see Table S1 for details of the XRD pattern) corresponds to an interlayer spacing of 0.335 nm. This value is in good agreement with the *d*-spacing of bulk graphite,[9–11] thus the density is the same one as for pure graphite. From the (002) peak, a thickness $\bar{t}$ of ~27 nm can also be calculated, which can be confirmed by the BET specific surface area (assuming that the lateral area of each particle is negligible because the particle diameter is much larger than the particle thickness): $\bar{t} \approx 2/(d_G \cdot S_{BET})$ = 36 nm. This is a clear evidence of the presence of GNP, and the GNP volume fractions inside nanocomposites can be certainly converted from the weight fractions by using the density of pure graphite, d_G.

It is possible to calculate the maximum effective Young's modulus of the filler, E_{GNP}^{eff}, from the value of the crystallographic thickness of GNP, as suggested by Gong *et al.*:[12]

$$E_{GNP}^{eff} = \frac{E_{graphene}}{\frac{n_l}{2} - k_i\left(\frac{n_l}{2} - 1\right)}$$

Equation S5.

where $E_{graphene} \approx 1000$ GPa, n_l is the average number of graphene layers stacked inside the GNP (~100 for our GNP), and k_i is a stress transfer efficiency factor between the layers (≈ 0.7). For our filler, the effective Young's modulus according to Equation S5 yields ~65 GPa. This is a reasonable value if compared to the results of Krzesinska *et al.*, who studied the elastic modulus of expanded graphite powders with different porosities using ultrasound measurements, and found that the maximum elastic modulus of completely compressed expanded graphite (without any porosity) is about 30 GPa.[7]

S.4 Influence of P&F cycles on the properties of neat LLDPE

The P&F technique consists of pressing a thermoplastic polymer with a nanofiller at a temperature slightly above the polymer's melting point, thus the polymer should recover its initial properties after cooling down to ambient temperature. It is worth noting that the P&F was performed in air, and in order to assess any effect of thermal degradation on the alteration of polymer properties, samples of pure LLDPE were prepared at 1, 50, 100, and 150 P&F cycles. Tensile tests revealed that the properties (Young's modulus, yield stress, and ultimate tensile stress) of pure LLDPE at different numbers of P&F cycles were relatively unaffected by the P&F technique up to 150 P&F cycles (see Figure S3). Therefore, the sample prepared at the first P&F cycle was used as reference sample for comparison with nanocomposites' properties.

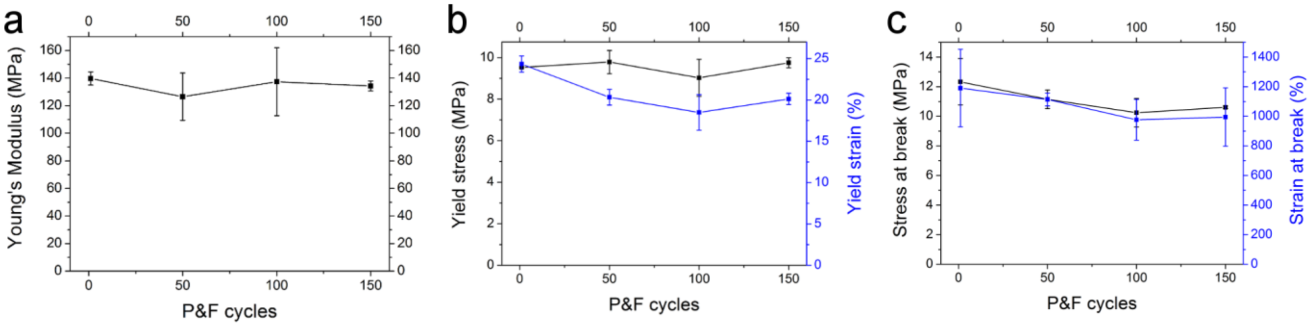

*Figure S3. Young's modulus (**a**), yield (**b**), and break point (**c**) of neat LLDPE samples prepared at different P&F cycles.*

The XRD pattern of pure LLDPE (Figure S1) shows two diffraction peaks around 21.6° 2θ and 23.8° 2θ due to the (110) and (200) reflections superimposed to an amorphous halo.[13,14] The crystallinity was ~33% for both samples prepared at one and 150 P&F cycles (Table S1). The crystallites size calculated from the (110) and (200) peaks were of 17 nm and 11 nm, for both samples. These findings suggest that the P&F technique up to 150 P&F cycles has little effect on the properties of neat LLDPE. Moreover,

Table S1 shows that a sample of LLDPE containing a small amount of GNP (0.21 vol.%) did not change its crystallinity up to 500 P&F cycles, confirming that the properties of LLDPE are not significantly influenced by the P&F technique.

S.5 Influence of P&F cycles on the properties of LLDPE and GNP inside nanocomposites

It was shown above how the P&F technique itself does not significantly influence the properties of neat LLDPE, however, the presence of GNP together with the effect of the pressing and folding cycles could change its crystallinity. This is important because LLDPE of higher crystallinity has an increased Young's modulus and yield stress, but lower tensile strength and elongation at break.[2]

Nanocomposites containing 4.8 vol.% of GNP showed that the LLDPE crystallite sizes and crystallinity increased slightly with the number of P&F cycles (Table S1). However, referring to the findings of Kundu *et al.*, a relative increase of ~8% in crystallinity found for the sample at 500 P&F is too low to significantly alter the mechanical properties of LLDPE.[2] Therefore, an eventual improvement of the nanocomposite's mechanical properties should be attributed mainly to an improved reinforcing efficiency of the nanofiller as a result of an improvement in nanofiller distribution and dispersion rather than an increase of polymer crystallinity.

We analysed these samples also by DSC (Figure S4), together with a highly loaded sample for comparison. We found that the nanofiller dispersion level slightly affect the crystallinity (see data in Table S4 for samples prepared after 50 and 200 P&F cycles). The amount of GNP has a similar effect (Table S4). However, these changes are negligible, so any improvement in the nanocomposite mechanical properties mast be caused by an increased nanofiller-matrix interface.

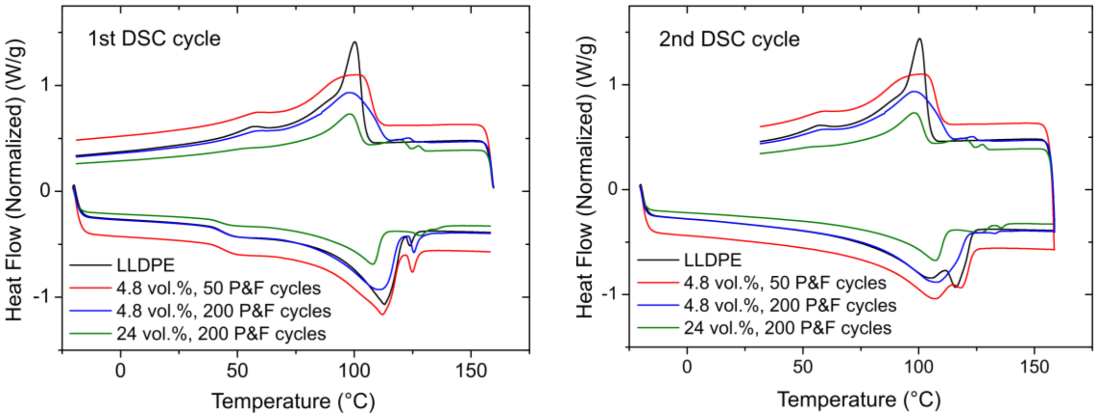

Figure S4. DSC analysis.

Table S2. Values found from the first DSC cycle of Figure S4.

SAMPLE	Heating			Cooling		
	Peak temp. (°C)	Enthalpy (J/g)	Onset temp (°C)	Peak temp. (°C)	Enthalpy (J/g)	Onset temp (°C)
4.8 vol%, 50 P&F cycles	112.19	70.319	89.88	102.57	63.516	109.83
4.8 vol.%, 200 P&F cycles	110.93	71.202	83.95	98.49	58.582	113.38
24 vol.%, 200 P&F cycles	110.93	71.202	83.95	98.49	58.882	113.38
LLDPE pristine	112.96	75.807	90.74	100.32	74.39	104.74

Regarding the GNP characteristics, the graphite diffraction peak did not change its position with the number of P&F cycles, meaning that the crystalline interlayer spacing and the density of GNP was unaffected by the P&F cycles. Likewise, since the (002) peak did not shift to lower 2θ values as it happens for graphite oxide,[11,15–18] no oxidation of GNP is expected to take place during the P&F process. Furthermore, the thickness of GNP remained the same with P&F cycles, meaning that there was no exfoliation of GNP during the process, thus any variation in the properties of the nanocomposites with

P&F cycles must be caused only by improved distribution and dispersion of the nanofiller, rather than an increase in GNP aspect-ratio.

All the above observations are confirmed by the samples of LLDPE containing 0.21 vol.% of GNP. No relevant changes in LLDPE crystallite sizes and crystallinity with the number of P&F cycles was present (Table S1), that is, the matrix properties are not influenced by the P&F technique. The graphite diffraction peak did not modify its position with the number of P&F cycles, meaning that the density of GNP was unaffected by the P&F cycles, and that GNP did not oxidize during the hot-pressing steps. Furthermore, the thickness of GNP remained the same with P&F cycles, viz. there was no exfoliation of GNP during the process.

S.6 Nanocomposites of LLDPE + 0.21 vol.% GNP at different P&F cycles: nanofiller distribution and microstructures

Figure S5a shows a macroscopic visualization of the effect of the P&F technique on the distribution of GNP throughout the specimen of a series of samples containing 0.21 vol.% of GNP. The colour of these samples became darker with P&F cycles because of better nanofiller dispersion and distribution. Figure S5b shows the microstructures of these nanocomposites at different P&F cycles. At low P&F cycles, the microstructures show large GNP agglomerates with a thickness nearly the same as the film sample, which decreased in thickness and width with P&F cycles. Eventually, at 500 P&F the particles were well distributed, dispersed and oriented parallel to the plane of the film samples.

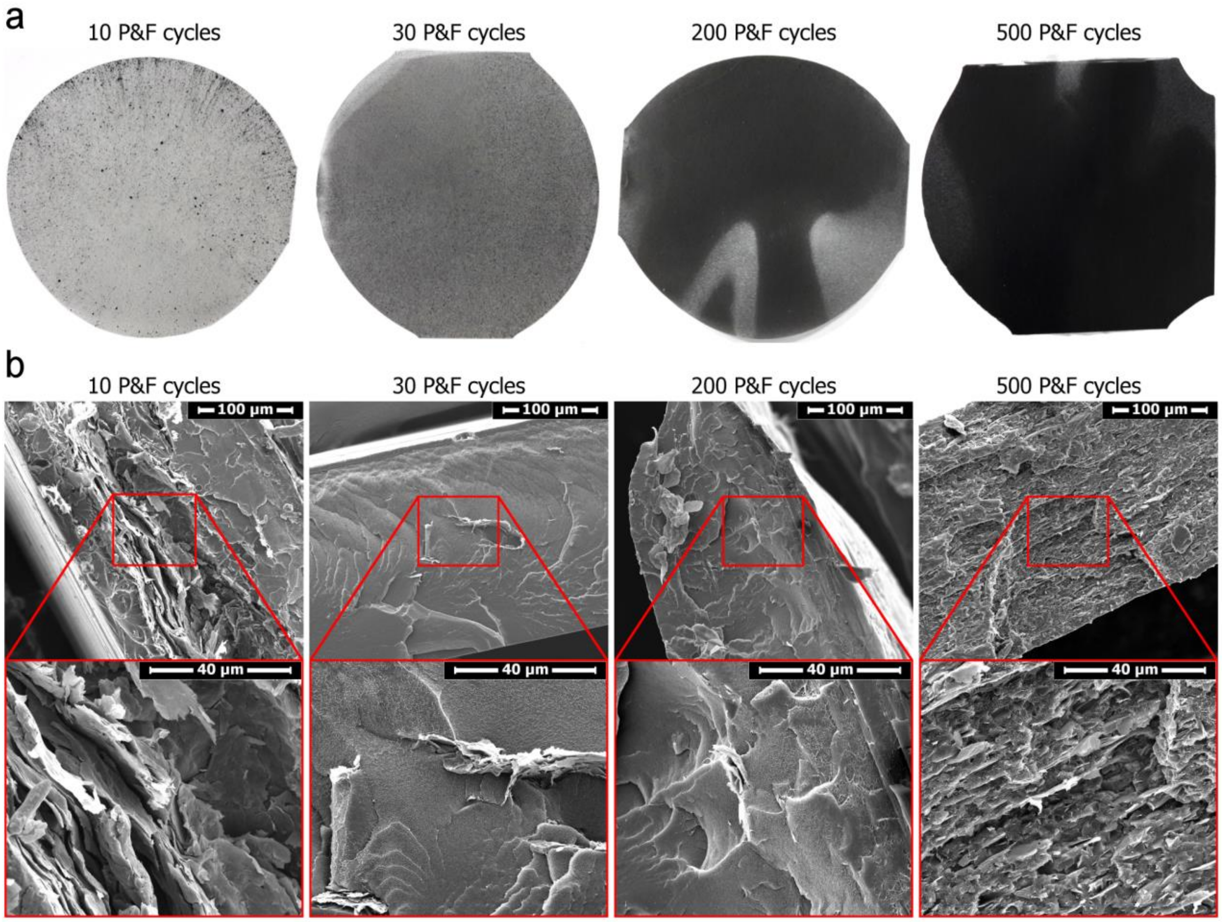

*Figure S5. Pictures (**a**) and SEM images (**b**) of the cross-sections of LLDPE + 0.21 vol.% GNP samples at different P&F cycles. The samples were about 8 cm in diameter, and 300 µm thick.*

S.7 Nanocomposites of LLDPE + 4.8 vol.% GNP at different P&F cycles

S.7.1 Filler agglomeration

The microstructure of nanocomposites of LLDPE + 4.8 vol.% GNP was systematically studied at different P&F cycles in order to find out the break-down of filler agglomerates during the P&F process. Figure S6a shows a macroscopic visualization of the effect of the P&F technique on the distribution of GNP throughout the specimen. The first P&F cycles break down initially the large agglomerates. Because of the high GNP concentration, the samples appeared homogeneous to the naked eye already after 20-30 P&F cycles, differently to the series of samples with lower GNP concentration (0.21 vol.%). Figure S6b shows how the microstructure of the same nanocomposites changes as a function of P&F cycles, whereas Figure S6c presents the geometrical mean values of aspect-ratio, diameter, and thickness of filler agglomerates obtained from the statistical distributions of the agglomerates measured from the samples' microstructures (see Figure S7). At 10 P&F cycles, there were large GNP agglomerates with thicknesses close to those of the disk film samples (ca. 300 µm). These agglomerates decreased in thickness and diameter very quickly with increasing P&F cycles up to 50 P&F cycles, with particles inside the agglomerates appearing to be mainly oriented parallel to the plane of the samples. Between 50 and 200 P&F cycles, it was difficult to find GNP agglomerates, and many dispersed particles appeared throughout the matrix volume. Eventually, the microstructure at 500 P&F cycles was clearly well-ordered with homogeneously distributed and well dispersed particles oriented parallel to the plane of the film samples.

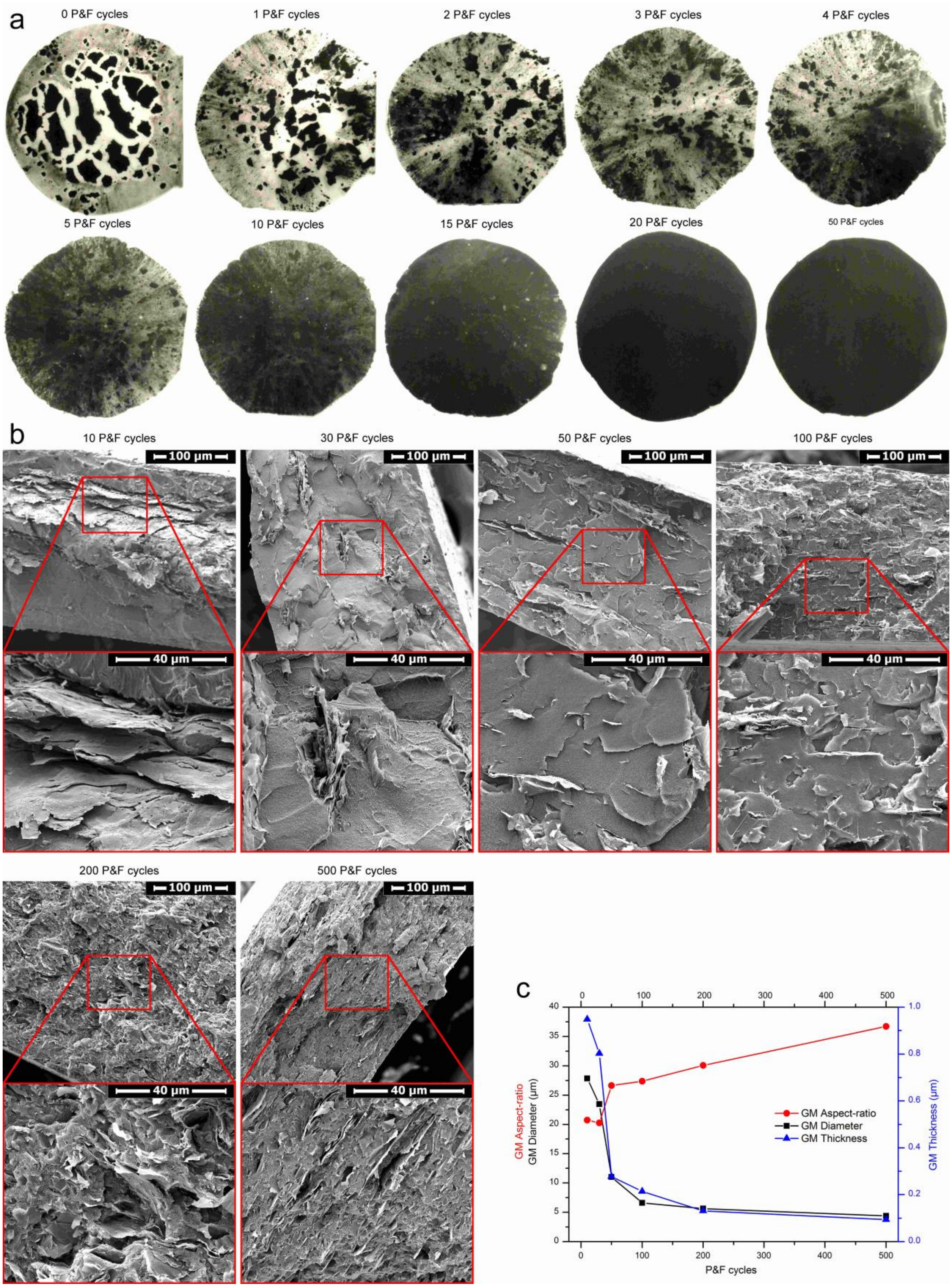
a
0 P&F cycles
1 P&F cycles
2 P&F cycles
3 P&F cycles
4 P&F cycles
5 P&F cycles
10 P&F cycles
15 P&F cycles
20 P&F cycles
50 P&F cycles
b
10 P&F cycles
30 P&F cycles
50 P&F cycles
100 P&F cycles
100 µm
40 µm
200 P&F cycles
500 P&F cycles
c
GM Aspect-ratio
GM Diameter (µm)
GM Thickness (µm)
P&F cycles
0
100
200
300
400
500
0
5
10
15
20
25
30
35
40
0.0
0.2
0.4
0.6
0.8
1.0

*Figure S6. (**a**) Pictures of LLDPE + 4.8 vol.% GNP samples at different P&F cycles, (**b**) SEM images of the cross-sections of LLDPE + 4.8 vol.% GNP samples, and (**c**) geometrical mean values of filler agglomerate's aspect-ratio, diameter and thickness as a function of P&F cycles. Film samples were about 8 cm in diameter, and 300 µm thick.*

Figure S7 shows the statistical distributions of diameter, thickness, and aspect-ratio of the agglomerates at different P&F cycles. The geometrical means of these distributions are reported in Table S3 together with their geometrical standard deviations, and displayed in Figure S6c. The mean diameter and thickness decreased drastically at the first ~50 P&F cycles (see also Figure S6c), and they further reduced to the size of single GNPs after 500 P&F cycles, meaning that a good dispersion of nanoparticles was reached at this high number of P&F cycles without any significant agglomeration. In fact, the geometrical mean thickness of the filler at 500 P&F cycles (~90 nm) is fairly close to the thickness of GNP (~30 nm). Conversely, the aspect-ratio of the agglomerates does not change significantly with the P&F cycles as diameter and thickness do, and it only doubles its initial value after 500 P&F cycles.

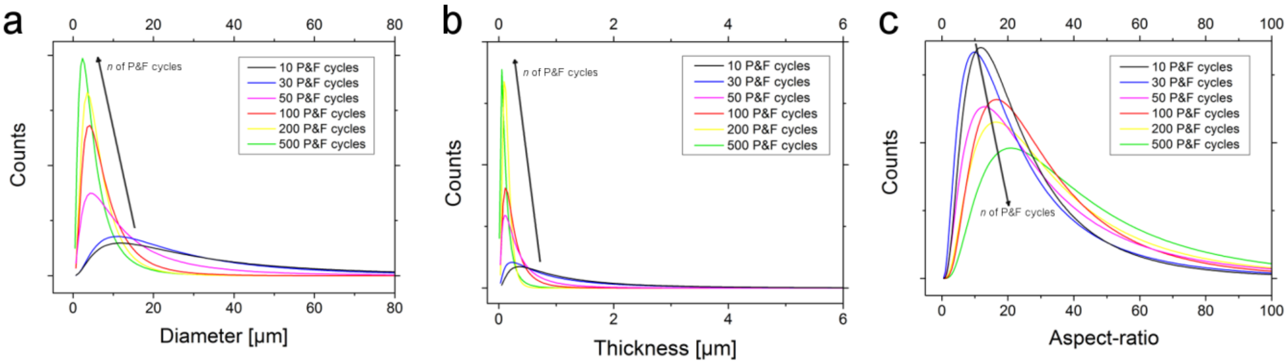

*Figure S7. Statistical distributions of (**a**) diameter, (**b**) thickness, and (**c**) aspect-ratio of filler agglomerates in nanocomposites of LLDPE + 4.8 vol.% GNP at different P&F cycles.*

Table S3. Geometrical means (GM) and geometrical standard deviations (GSD) related to the distributions of Figure S7.

P&F cycles	Diameter		Thickness		Aspect-ratio	
	GM (µm)	GSD	GM (µm)	GSD	GM	GSD
10	27.9	2.54	0.948	2.70	20.7	2.12
30	23.5	2.39	0.803	3.06	20.2	2.33
50	11.0	2.58	0.278	2.64	26.6	2.34
100	6.60	2.02	0.214	2.15	27.4	2.04
200	5.64	1.96	0.131	1.66	30.1	2.18
500	4.37	2.21	0.093	2.36	36.7	2.11

S.7.2 Fracture morphology

Figure S8 shows the fracture surfaces of LLDPE + 4.8 vol.% GNP samples prepared at different P&F cycles. At low number of P&F cycles, the fracture surfaces show GNP agglomerates with thicknesses almost as thick as the film samples (Figure S8a). Such large agglomerates were not visible in cryogenically broken specimen. This can be explained by the fact that failure was initiated by the widest agglomerates because of stress concentrations in the polymer matrix (the agglomerates cannot carry the applied load because they are not a continuum body). In fact, samples prepared below 50 P&F cycles typically showed some GNP dust coming from the fracture surface, indicating that the GNP powder was not fully embedded in the polymer. The consequence of this was that the tensile strength of these samples was lower than that of pure LLDPE. For example, the sample prepared at 10 P&F cycles contained some wide agglomerates up to ~1/4 of the fracture surface area, and its stress at break was 7 MPa (stress at break of pure LLDPE was 9.5 MPa). If the cross-section relative to LLDPE is used for the calculation of the stress at break, than the stress at break gives ~7 MPa / (1–1/4) = 9.3 MPa, which is the stress at break of pure LLDPE. Samples prepared above 150 P&F cycles did not present any GNP agglomerates in the fracture surfaces, and their stresses at break were higher than that of pure LLDPE.

Moreover, the fracture surface of these samples appeared smooth and regular with short LLDPE fibrils disposed in layers (Figure S8b). On the contrary, samples prepared at low P&F cycles presented irregularly shaped fracture surfaces, with wide and long strained LLDPE fibrils, which were similar to those observed in pure LLDPE samples.

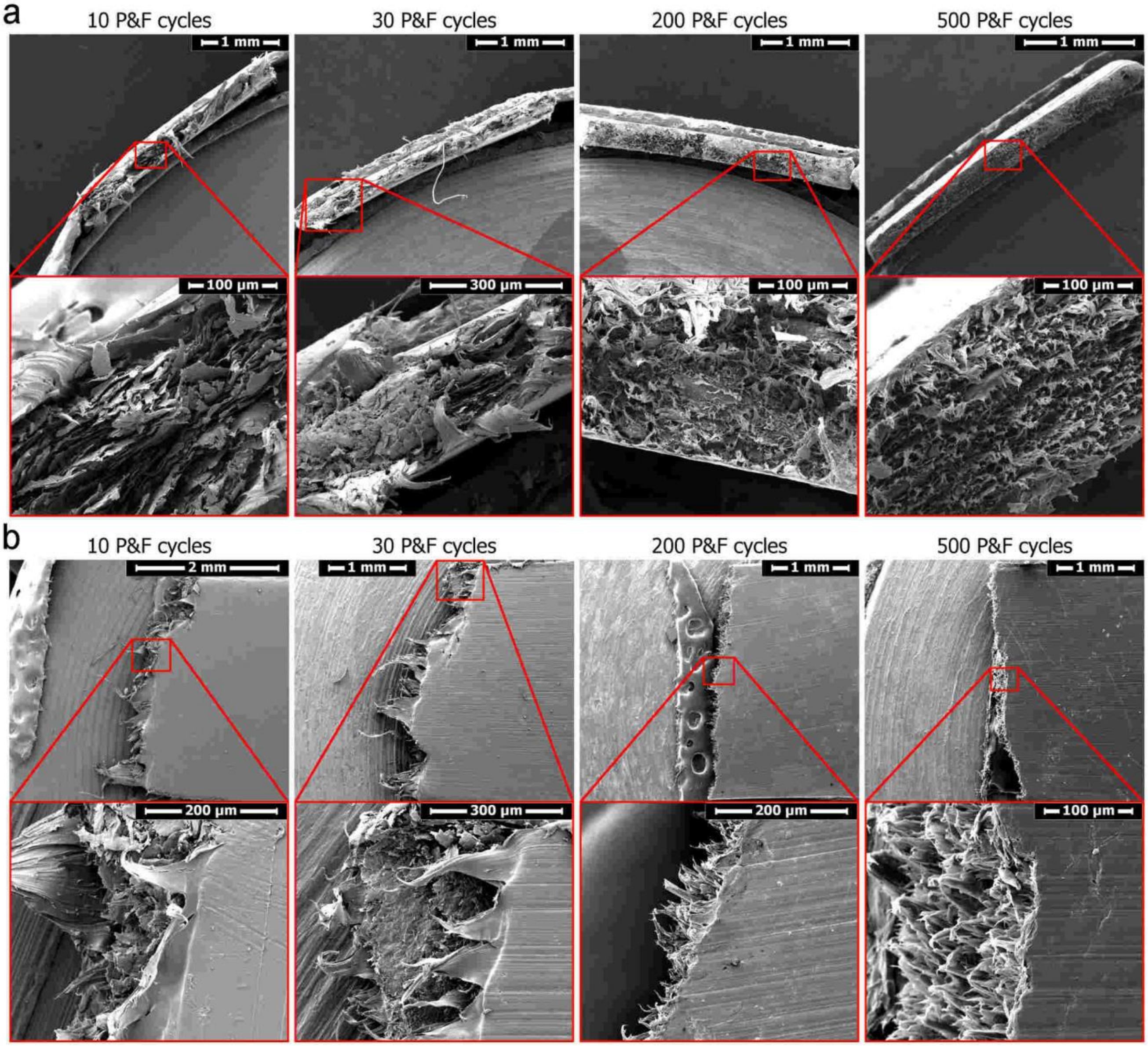

*Figure S8. Front view (**a**) and side view (**b**) of the tensile fracture surfaces of LLDPE + 4.8 vol.% GNP samples prepared at different P&F cycles.*

S.8 Nanocomposite of LLDPE + 4.8 vol.% GNP prepared by melt-blending

Figure S9 shows the microstructure of a LLDPE nanocomposite prepared by melt-blending containing 4.8 vol.% of GNP. Different from the microstructures of nanocomposites prepared by P&F, the particles appear more 3D randomly oriented, but no large agglomerates are present, as in samples prepared above 200 P&F cycles.

Tensile tests revealed a mechanical reinforcement (E_c/E_m) of 1.4 ± 0.3, which is equivalent to samples prepared by 100 P&F cycles, a yield stress of 9.9 ± 0.9 MPa and an ultimate tensile stress of 9.4 ± 1.1 MPa, similar to samples prepared at 150 P&F cycles. The tensile fracture surface (Figure S9) is straight as it happens for P&F samples above 100 P&F cycles, and the LLDPE fibrils after failure have a similar morphology of those observed in the P&F sample prepared at 200 P&F cycles.

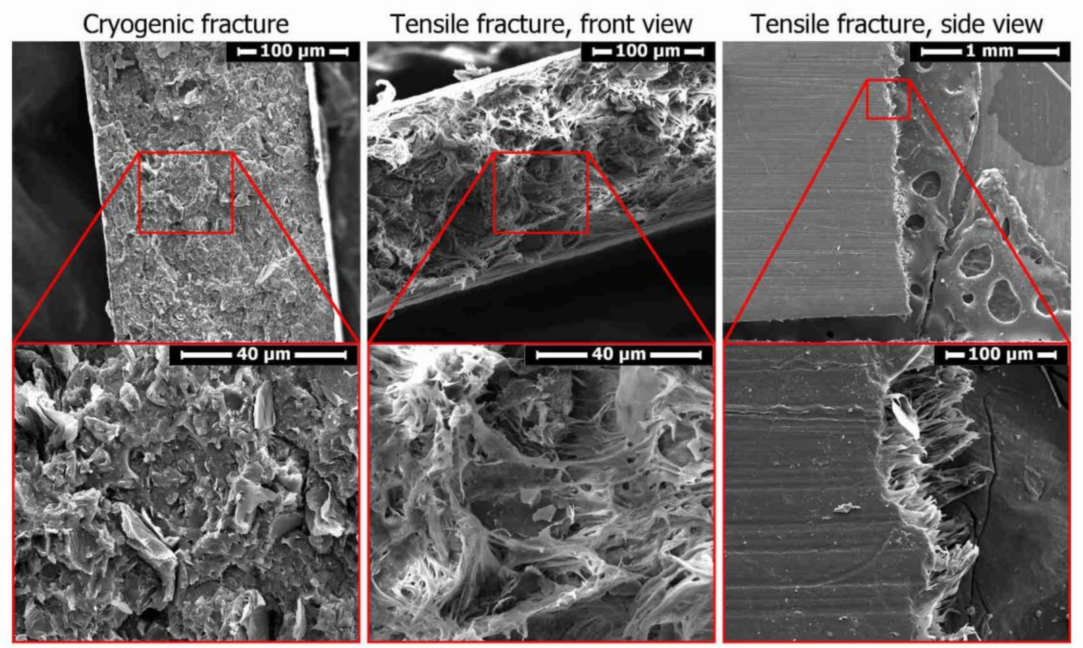

Figure S9. Cryogenic and tensile fracture surfaces of a LLDPE + 4.8 vol.% GNP sample prepared by melt-blending and compression moulding.

S.9 Influence of GNP loading on the properties of GNP and LLDPE inside nanocomposites prepared at 200 P&F cycles

As reported in Table S1, the LLDPE crystallite sizes remained almost the same for samples prepared at 200 P&F cycles containing three different amounts of GNP (0.21, 4.8, and 35 vol.%): there was only a small decrease from 17 nm to 15 nm for the crystallite size related to the (110) peak of the sample containing 35 vol.% of GNP. The LLDPE crystallinity increased with the amount of GNP. These findings are in contrast with what is reported in literature: the addition of nanofiller slightly increased the LLDPE crystallite sizes,[1] and decreased the degree of crystallinity,[1,13] because of a random interface between nanofiller and matrix, which "inhibited the ordered crystalline structure of the polymer chains".[1] Other studies indicated that the LLDPE crystallinity calculated from differential scanning calorimetry (DSC) measurements did not change with the amount of GNP,[19] or with the amount of graphene.[18] Therefore, the P&F technique might help the LLDPE polymer chains to arrange themselves in a crystalline structure among graphite nanoparticles. However, referring to the findings of Kundu *et al.*, a relative increase of ~22% in crystallinity compared with pure LLDPE was found for the sample containing 35 vol.% of GNP is too low to significantly alter the mechanical properties of LLDPE.[2]

Eventually, the position of the graphite (002) peak and the thickness of GNP remained the same as a function of the amount of GNP in the samples, meaning that there was no change in the intrinsic properties of GNP during the processing of these nanocomposites.

Representative stress-strain curves of nanocomposites prepared at 200 P&F cycles with different GNP loadings are presented in Figure S10. The strain at break abruptly decreases with the GNP amount, and the sample containing 35 vol.% GNP clearly does not show any yield before fracture.

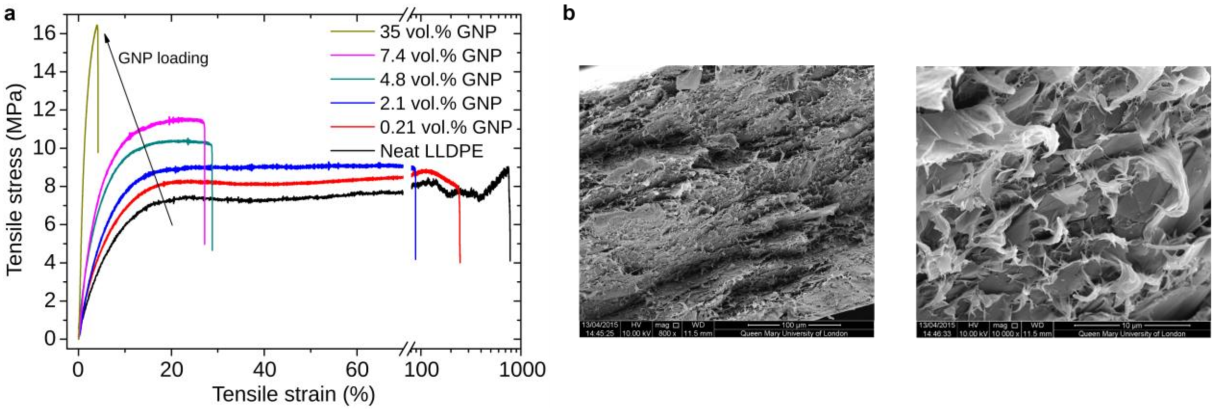

*Figure S10. (**a**) Representative stress-strain curves of GNP-LLDPE nanocomposites prepared with 200 P&F cycles and different GNP loadings. (**b**) SEM cross-sections of LLDPE + 35 vol.% GNP after 200 P&F cycles: the microstructure contains aligned and well dispersed GNP despite the high GNP concentration.*

S.10 Rheology study

Viscosity of P&F samples containing 4.8 vol.% GNP at different temperatures

The P&F technique was performed at a temperature (120 °C) really close to the melting point of the polymer (116 °C), differently from melt-blending techniques that use temperatures around 190 °C for LLDPE. This has a consequence on the viscosity of the samples, which results much higher than what it should be if the samples were processed at higher temperatures.

The graphs below show the viscosity of the P&F samples containing 4.8 vol.% GNP at 120 °C, 140 °C, and 180 °C. Note that the viscosity of neat LLDPE decreases from ~4.000 Pa.s at 120 °C to ~350 Pa.s at 180 °C.

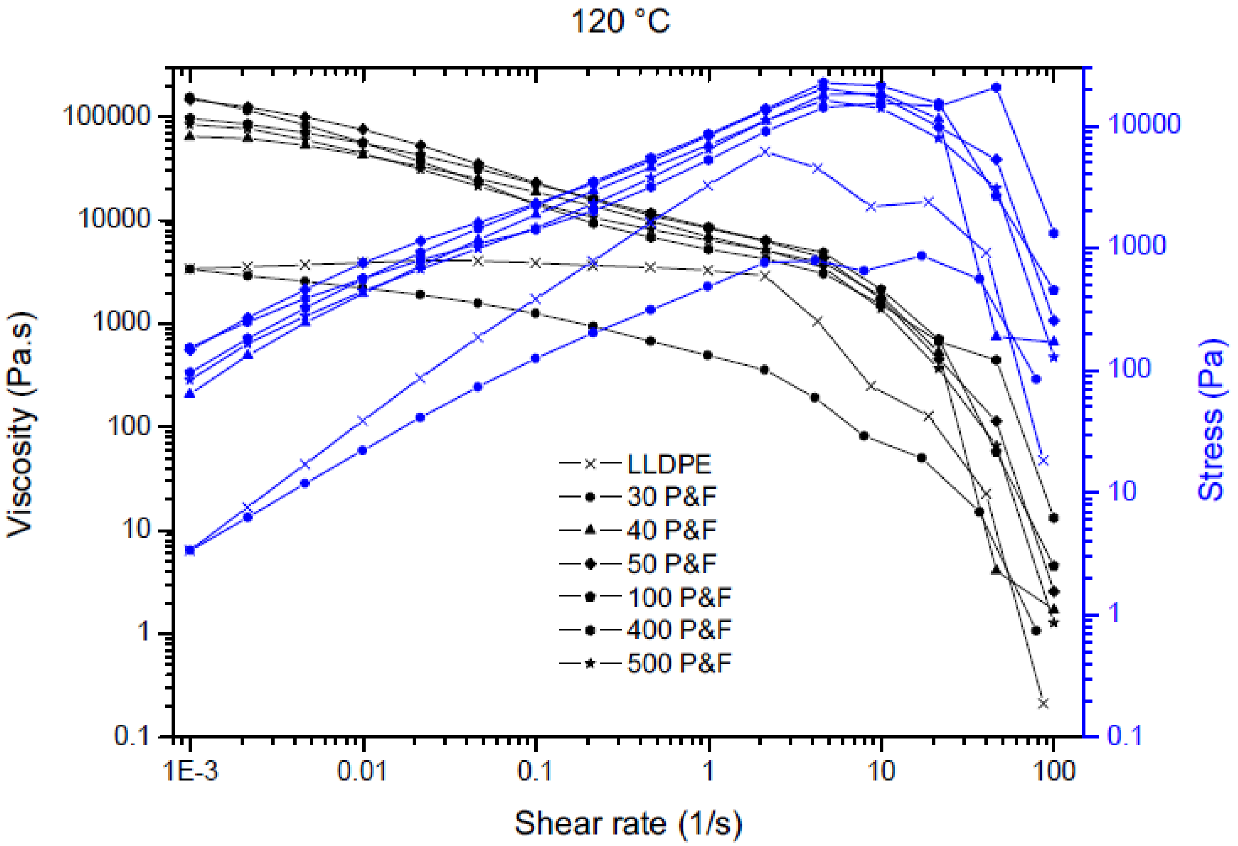

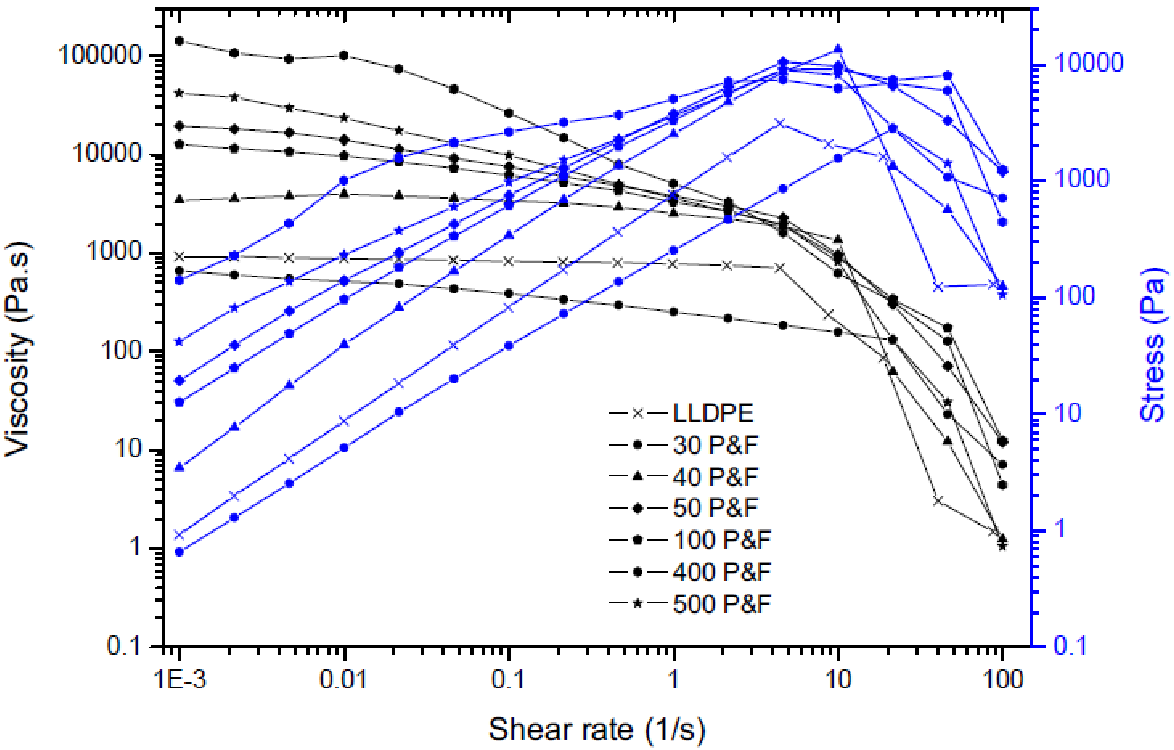
140 °C

Viscosity (Pa.s)
100000
10000
1000
100
10
1
0.1
1E-3
0.01
0.1
1
10
100
Shear rate (1/s)
Stress (Pa)
10000
1000
100
10
1
0.1
LLDPE
30 P&F
40 P&F
50 P&F
100 P&F
400 P&F
500 P&F

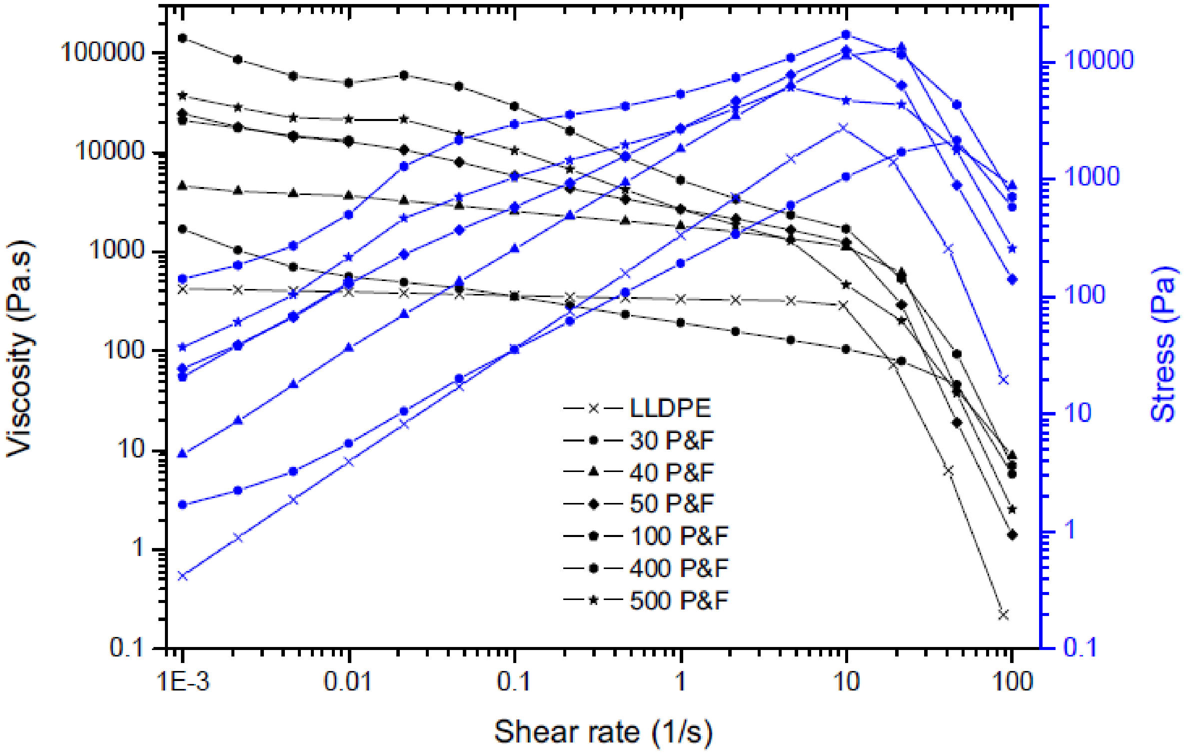
180 °C

Viscosity (Pa.s)
100000
10000
1000
100
10
1
0.1
1E-3
0.01
0.1
1
10
100
Shear rate (1/s)
Stress (Pa)
10000
1000
100
10
1
0.1
LLDPE
30 P&F
40 P&F
50 P&F
100 P&F
400 P&F
500 P&F

It is interesting to note that, for all the considered temperatures, the viscosity of the samples prepared with less than 40 P&F cycles is lower than the viscosity of neat LLDPE. Considering that microstructure of nanocomposites prepared with less than 50 P&F cycles presents agglomerates that are bigger than the dimensions of the initial GNP powder macro particles and that these samples also lost some GNP powder from their tensile fracture surfaces, it is fair to infer that such agglomerates act as a lubricant to the molten LLDPE matrix, lowering the viscosity of sample compared to that of neat LLDPE.

Samples prepared with more than 40 P&F cycles show increasing viscosity with the number of P&F cycles. When analysed at 120 °C, however, these samples do not show a remarkable increase of the viscosity with the number of P&F cycles as when they were analysed at higher temperatures do.

A common feature of the samples tasted at different temperatures is the decrease of the shear stress over a range of shear rates in which also the viscosity decreases. This can be explained by sample slippery on the rheometer walls.

Comparison with the literature

LLDPE usually found in literature has melt flow index (MI) of ~1 g/10min or less.[20–24] The MI of the LLDPE grade (Flexirene MS 20 A) used in our P&F project has a much higher MI: 26 g/10min. This must be due to a lower molecular weight of our polymer compared to the grades of LLDPE usually employed.

Consequently, the viscosity data found in literature (usually tested at 190 °C) are about 15-25 times higher than our LLDPE. However, a sample with MI of 50 g/min was reported to have a viscosity that was about half of the viscosity of our LLDPE.[23] Therefore, the viscosity measured for our LLDPE must be correct.

Moreover, literature data[20–24] show a decrease in the viscosity of about one order of magnitude within a rate of shear rate of 100-1000 1/s. Our LLDPE, conversely, shows this reduction over a range of 10-100 1/s (at 180 °C). This might be due both to a low mean molecular weight and to a wide molecular weight distribution of our LLDPE.

S.11 Model derivation

S.11.1 Estimation of the shear-rate during P&F

We approximate the flow during the P&F process as an axisymmetric squeeze flow between two parallel plates located at a distance 2*h*. The radius of the sample when the gap height is 2*h* is denoted by *R*.

In a cylindrical coordinate system with origin located at the midpoint between the plates, the radial velocity profile corresponding to a power-law fluid with constitutive equation $\tau_{rz} = m\left(-\frac{\partial v_r}{\partial r}\right)^n$ squeezed between two no-slip surfaces is[25]

$$v_r = \left(\frac{-\dot{h}r}{h}\right) B_n \left[1 - \left(\frac{z}{h}\right)^{1+1/n}\right]$$

Equation S6.

where $B_n = \frac{2n+1}{2n+2}$. The local shear rate is

$$\dot{\gamma} = \frac{\partial v_r}{\partial z} = \left(\frac{-\dot{h}r}{h^2}\right) B_n (1 + 1/n) \left(\frac{z}{h}\right)^{1/n}$$

Equation S7.

and the volume-averaged shear rate magnitude over the sample is

$$\langle\dot{\gamma}\rangle = \frac{1}{\pi R^2 h} \int_{r=0}^{R} \int_{z=0}^{h} |\dot{\gamma}|\, 2\pi r dr dz = \frac{2}{3} B_n \frac{\dot{h}R}{h^2}$$

Equation S8.

For *n* > 0, B_n varies weakly with *n* (for a shear thinning fluid, *Bn* varies from B_n = 3/4 for *n* = 1 to B_n = 1/2 for *n* = 0). In terms of orders of magnitude, we can thus write

$$\langle\dot{\gamma}\rangle = c_n \frac{\dot{h}R}{h^2}$$

Equation S9.

where c_n is a constant of order 1. In the case of slip surfaces, the flow is a uniform biaxial extensional flow and the average generalised shear rate is $\langle\dot{\gamma}\rangle = \sqrt{3}\frac{\dot{h}}{h}$.[26] Because $R/h \gg 1$, the average shear rate in the perfect slip case can be order of magnitude smaller than in the no-slip case.

In our experiment $|\dot{h}| \simeq 1.8$ mm/s, and h varies from 1 mm to 0.25 mm. During compression, the radius of the sample varies from 2 cm to 4 cm. In the case of slip surfaces, the average shear rate thus varies from 3 to 12 s^{-1} during compression. In the case of no-slip surfaces, the average shear rate varies from 36 s^{-1} to 1152 s^{-1}, where we have taken $c_n = 1$ for simplicity. The experimental case will likely be between the no-slip and the perfect slip case. We take $\langle\dot{\gamma}\rangle \sim 10$ s^{-1} and $\langle\dot{\gamma}\rangle \sim 1000$ s^{-1} as values representative of the initial and final stages of compression.

Fitting the LLDPE sample data for 10.7 wt.%, we obtain a power-law for the viscous stress $\tau \simeq \kappa\langle\dot{\gamma}\rangle^n$, where $\kappa \approx 500$ (in SI units) and $n \approx 0.75$. Using the reference values, the average stress is estimated to vary roughly between 3 KPa and 90 KPa during compression, depending on the adhesion of the polymer to the confining walls.

To evaluate whether exfoliation can take place, we need to compare the flow-induced stresses to the yield stress of the aggregate τ_y. For percolating suspensions, the following model has been recently proposed[27] that seems to fit well experimental data for graphene suspensions:

$$\sigma_y \simeq \frac{4}{3}\frac{\Gamma}{D_p}\phi_c^2 f(\phi/\phi_c)$$

Equation S10.

where ϕ is the volume fraction, ϕ_c is the volume fraction at the percolation threshold, $\Gamma \simeq 70$ mN/m is the graphene-graphene surface energy, D_p is the platelet diameter, and $f = \frac{(\phi/\phi_c - 1)^{2.5}}{(\phi/\phi_c + 1)^{0.5}}$. The percolation threshold can be estimated as $\phi_c \simeq 1.5t/D_p$,[27] where t is the thickness of each platelet. For $D_p/t = 26$, close to the initial aspect-ratio of the microplates embedded into the polymer, we get $\phi_c \simeq 0.057$. For $D_p = 9.4$ µm, $\frac{\Gamma}{D_p}\phi_c^2 \simeq 2.4$ Pa. Accounting for the *f* factor, even assuming that the local volume fraction within a macro-aggregate is 10 times the percolation threshold ($\phi_c \simeq 0.57$), the aggregate yield stress is roughly 0.24 KPa, much less than the applied viscous stress. The formula above is probably not very accurate for dense macro-aggregates for which ϕ is close to 1. In this case, using basic fracture mechanics arguments, one may write the order of magnitude of the force required to break the contact between each platelet in the macro-aggregate as ΓD_p. The force acts over an area D_p^2, so the corresponding stress is of the order of $\sigma_y \sim \Gamma/D_p$, which is about 0.74 KPa. Also this estimate gives a yield stress value much smaller than the applied viscous stress.

S.11.2 Modelling of nanofiller dispersion and nanocomposite properties as a function of nanofiller dispersion level

The increase in interfacial area, *A(n)*, between GNP and LLDPE due to the distribution and dispersion after a particular interval of P&F cycles depends on the following aspects:

- Dimension of the considered interval of P&F cycles, Δn;
- Distribution rate, *I*, which is a constant that describes how the polymer melt can distribute the particles during the hot-pressing step;
- Difference between the total surface area of the particles, A_p, and the actual interfacial area with the matrix: $A_p - A(n)$. In fact, when all particles are in contact with the matrix ($A(n) = A_p$, *i.e.* perfect nanofiller dispersion) it is impossible to further increase the nanofiller-matrix interface, and distribution is the only phenomena that occurs in the P&F process.

In mathematical terms, this corresponds to the following equation:

$$\Delta A(n) = \Delta n \cdot I \cdot \left(A_p - A(n)\right)$$

Equation S11.

If $\Delta n \rightarrow 0$, the previous expression becomes a differential equation. Supposing that A_0 is the initial interfacial area at $n = 0$ P&F cycles, then a particular solution of this differential equation is the following:

$$A(n) = A_p - (A_p - A_0)e^{-I \cdot n}$$

Equation S12.

The total surface area A_p can be calculated from the specific surface area of GNP and the amount of GNP introduced in each sample. For example, the sample containing 4.8 vol.% of GNP was prepared with ~0.16 g, hence $A_p \approx 40000$ cm^2. The initial interfacial area A_0 can be easily estimated by measuring the percentage of sample area covered by particles from the picture taken at 0 P&F cycles, and multiplying this by twice the total sample area (~100.5 cm^2). For the sample of 4.8 vol.% of GNP, $A_0 \approx 34$ cm^2.

For situations where the nanofiller is not well dispersed, *i.e.* until $A(n) \neq A_p$, it is not possible to completely use its reinforcing effect as predicted by the Halpin-Tsai model (reported in Section S.13.1). Indeed, the shear-lag theory of Cox states that there is load transfer from matrix to filler only when they are in perfect contact with each other. In other words, when the nanofiller is not well dispersed, its particles inside the agglomerates do not contribute to the properties of the nanocomposite. As a consequence, it is possible to exploit the volume fraction of the nanofiller only when it is completely in contact with the matrix, *i.e.* when $A(n) = A_p$. Thus, the effect of a not perfect dispersion is that the effective volume fraction, V_p^{eff}, is lower than the nominal one, V_p:

$$V_p^{eff} \equiv D \cdot V_p$$

Equation S13.

where D is a dispersion factor, which ranges from 0 (nanofiller and matrix are completely not in contact) to 1 (nanofiller perfectly dispersed and completely in contact with the matrix). How the dispersion factor varies with the interfacial area between nanofiller and matrix is challenging, and in first approximation, we could define the following definition:

$$D \approx \frac{A(n)}{A_p} = 1 - \frac{(A_p - A_0)e^{-I \cdot n}}{A_p}$$

Equation S14.

so when $A(n) = 0$ (no contact between nanofiller and matrix), then also D is zero, and when $A(n) = A_p$ (nanofiller perfectly dispersed and in contact with the matrix), than $D = 1$.

In general, any property as a function of nanofiller dispersion can be approximated by the following relationship:

$$P(D) \approx P_0 + (P_{th} - P_0) \cdot D$$

Equation S15.

where P is a particular property of the nanocomposite; P_0 is the property at $D = 0$; and P_{th} the expected value of the property when the nanofiller is perfectly dispersed ($D = 1$). For example, for the mechanical reinforcement $P = E_c/E_m = R$, $P_0 = 1$, and $P_{th}–P_0 = \eta\cdot(\zeta+1)\cdot V_p$ (after expansion of the Halpin-Tsai model in a first-order Maclaurin series). Similarly, for the yield stress $P = Y$, $P_0 = Y_m$ (yield stress of LLDPE), and $Y_{th}–Y_0 = Y_m\cdot(B_{Puk}–3.5)\cdot V_p$ (after expansion of the Pukanszky model, reported in Section S.13.2, in a first-order Maclaurin series).

By introducing the fitting parameters found for our mechanical reinforcement data (Section S.11.5) inside these relationships between Equation S15 and the Halpin-Tsai model, we can back-calculate a nanofiller aspect-ratio ξ of ~55. This result is close to $\xi_{th} = 38$ found from agglomerates aspect-ratio fit (Section S.11.5), and to $\xi = 43$ from the fitting of the reinforcement of nanocomposites containing different GNP loadings and prepared at 200 P&F cycles (see main article). Note that for the back-calculation we used a GNP and LLDPE moduli of 1 TPa and 140 MPa, respectively. However, the GNP modulus could be lower than 1 TPa (see Section S.3), but even using a modulus as low as ~65 GPa the final value of the aspect-ratio does not change significantly (~60 instead of ~55).

Similarly, by introducing the fitting parameters found for the yield data (Section S.11.5) inside the relationships between Equation S15 and the Pukanszky model, we can back-calculate an interaction parameter B_{Puk} of ~14. This result is similar to the value found from the fitting of yield stress of nanocomposites containing different GNP loadings and prepared at 200 P&F cycles (see main article).

Regarding the electrical conductivity, this property is strongly dependent on the distance between the particles of the nanofiller because the overall electrical conduction happens by electron tunnelling between the particles. Thus, the electrical conductivity could show a percolation behaviour, and its variation with nanofiller dispersion depends on the following aspects:

- Dimension of the considered interval of nanofiller dispersion, ΔD;
- a', which is a constant correlated to the velocity of the conductivity change with the inter-particle distance;
- Critical nanofiller dispersion, D_c, at which there is a quick change in electrical conductivity (for instance, from insulator to conductor), namely by the difference $D - D_c$;
- Asymptotic conductivity, σ_{th}, that is the theoretical conductivity when the nanofiller is perfectly dispersed (D=1) or when there is a drop-down of the percolation network due to inter-particle distances greater than the critical distance for electron tunnelling between particles. This corresponds to the difference $\sigma_{th} - \sigma$.

These aspects can be translated into a differential equation that can be solved to give the following relationship between conductivity and nanofiller dispersion:

$$\sigma(D) = \sigma_{th} + (\sigma_M - \sigma_{th}) \cdot e^{-a(D-D_c)^2}$$

Equation S16.

with D given by Equation S14. We believe that Equation S16 provides a more realistic description of the electrical conductivity than Equation S15.

S.11.3 Dispersion-factor for a melt-blending process

We note that Equation S14 can be adapted for the melt-blending process. In this case, *n* should be replaced by the processing time. The *I*-factor not only depends on types of nanofiller and polymer used, but also on shear rate and stress, and polymer viscosity. Moreover, the *I*-factor can be influenced by some aspects that can deteriorate both the polymer and the nanofiller, such as the delivered extrusion power, and processing time.

S.11.4 Dispersion-factor for a solution-mixing/casting process

Differently from our P&F process or melt-blending techniques, solution-mixing followed by solution casting is a bottom-up technique. Indeed, nanocomposites are formed by the joining of nanoparticles with polymers that happens directly at the nanoscale level when solvent is started being removed (solution casting), and grow up in volume with solvent evaporation. To understand how nanofiller can agglomerate during this process, we can refer to the work of Li and Kim,[28] who developed a model based on the average interparticle distance (IPD). Their model is used to quantify the critical nanofiller volume fraction for electrical percolation. Electrical percolation happens when the distance between the particles of nanofiller, d_{IP}, equals the critical length for electron hopping to occur from one particle to another one (and it is usually assumed around 10 nm).[28] Since the interparticle distance depends on the amount of nanofiller, Li and Kim could derive some expressions for the critical volume fractions for electrical percolation in nanocomposites containing different types of nanofillers and oriented in different distributions.

Similarly, we can find the critical volume fractions that start giving nanofiller agglomeration during solution casting. We just need to set the interparticle distance, d_{IP}, equal to zero. In this way, we can modify the expressions derived by Li and Kim to calculate the critical volume fraction for agglomeration in nanocomposites containing, for example, nanoplatelets organized in a planar distribution:

$$V_{p\_2D}^{c} = \frac{2\pi}{\xi}$$

Equation S17.

or nanoplatelets organized in a 3D random orientation:

$$V_{p\_3D}^{c} = \frac{27\pi}{4\xi}$$

Equation S18.

In both cases, the critical volume fractions depend on the aspect-ratio, ξ, of the nanoplatelets.

For nanofiller amounts higher than V_p^c, the nanoparticles are not completely in direct contact with the polymer matrix, so we can find a contact area, A_g, between them. In other words, A_g corresponds to the agglomeration contact area. The variation of this nanofiller agglomeration area may depend on the following factors:

- Variation in nanofiller volume fraction, ΔV_p;
- Difference between the total surface area of the nanoparticles, A_p, and the actual agglomeration contact area: $A_p - A_g$. In fact, when all nanoparticles are completely agglomerated, it is impossible to further increase the agglomeration contact area;
- s, which is a parameter that describes how fast the nanoparticles agglomerate. This parameter may be influenced by different aspects such as the nature of the nanoparticles (if nanoparticles interact with one another with strong Van der Waals forces, they are likely to agglomerate quickly); functionalization of nanoparticles or polymers (if nanoparticles can be easily bonded to the polymer matrix, it will be less likely that they agglomerate); and nanoparticle aspect-ratio (the higher the aspect-ratio, the more difficult is to control the configuration of the nanoparticles, and the more likely the nanoparticles crumple or fold).

These aspects can be translated into a differential equation that can be solved considering that when $V_p = V_p^c$, then A_g is zero:

$$A_g(V_p) = A_p - A_p e^{-s(V_p - V_p^c)}$$

Equation S19.

Eventually, considering that the nanofiller-polymer contact area is given by the difference $A_p - A_g$, we can derive the following dispersion factor for a solution-mixing/casting process:

$$\begin{cases} D_{s-m/c}(V_p) = 1 & \text{for } V_p \leq V_p^c \\ D_{s-m/c}(V_p) = e^{-s(V_p - V_p^c)} & \text{for } V_p > V_p^c \end{cases}$$

Equation S20.

By introducing this *D*-factor for the solution-mixing/casting process inside Equation S13, we can predict or describe the mechanical behaviour of casted nanocomposites affected by nanofiller agglomeration.

S.11.5 Model fitting of P&F data

We fitted the GNP agglomerate observations of Figure 1e and the mechanical properties of Figure 2b with Equation S15, and the electrical conductivities of Figure 2c with Equation S16 (all these figures are relative to the main article). In both cases, we used the P&F-related *D*-factor (Equation S14), thus we could find the distribution-rate *I* of the P&F process, useful to quantify the nanofiller dispersion level at different P&F cycles. Table S4 reports the fitting parameters for each property. As expected, the *I*-factor of the P&F process results to be independent of the analysed property. However, we decided to calculate a mean distribution-rate *I* of $(3.3 \pm 1.4)\cdot 10^{-3}$ from the mechanical and electrical properties only, because the GNP agglomerate measurements could have been affected by some obvious problems of images resolution and operator-related errors.

Table S4. ***Fitting parameters of the properties of LLDPE + 4.8 vol.% GNP nanocomposites for our nanofiller dispersion models.***

Observable property, *P*	P&F-related dispersion model (Equation S14)	Predictive model of Equation S15		Predictive model of Equation S16		Adjusted R^2 of the fit
	I-factor	P_0	P_{th}	n_c *	a	
GM aspect-ratio, ξ	$5\cdot 10^{-3}$	19.5	38	-	-	0.86
GM diameter, *d*	$29\cdot 10^{-3}$	38 µm	4.9 µm	-	-	0.89
GM thickness, *t*	$27\cdot 10^{-3}$	1.1 µm	112 nm	-	-	0.74
Reinforcement, *R*	$2.5\cdot 10^{-3}$	1.02	2.8	-	-	0.79

Yield stress, *Y*	$3.9\cdot10^{-3}$	8.32 MPa	12.3 MPa	-	-	0.98
Stress at break, *B*	$5.5\cdot10^{-3}$	6.76 MPa	11.7 MPa	-	-	0.997
In-plane electrical conductivity, $\sigma_{i\text{-}p}$	$2.0\cdot10^{-3}$	-	-	96	114	0.80
Out-of-plane electrical conductivity, $\sigma_{o\text{-}o\text{-}p}$	$2.5\cdot10^{-3}$	-	-	97	84	0.64

* n_c is the critical number of P&F cycles, which is related to the critical nanofiller dispersion level, D_c, through Equation S14.

S.11.6 Another approach to estimate the distribution rates

The rate of a nanofiller distribution inside a certain matrix during the P&F dispersion process can be quickly calculated by using the initial nanofiller/matrix contact area (A_0), and the contact area after *n* P&F cycles (A_n):

$$I = \frac{1}{n} ln\left(\frac{A_p - A_0}{A_p - A_n}\right)$$

Equation S21.

The total nanofiller surface area (A_p) can be calculated using the specific surface area (*S*), and the amount *m* of nanofiller introduced inside a sample:

$$A_p = S \cdot m$$

Equation S22.

Both A_0 and A_n could be estimated by measuring the percentage, *C%*, of sample area covered by nanofiller from the optical pictures of the sample:

$$A_{0,n} = 2 \cdot sample\ area \cdot C\%$$

Equation S23.

Figure S11 shows the method used to calculate the sample area and *C%* from the optical pictures. A_n is more accurate if *C%* is measured at low (<5) P&F cycles, *i.e.* when the probability of having an overlapping of nanofiller agglomerates is low, thus A_n will not result underestimated.

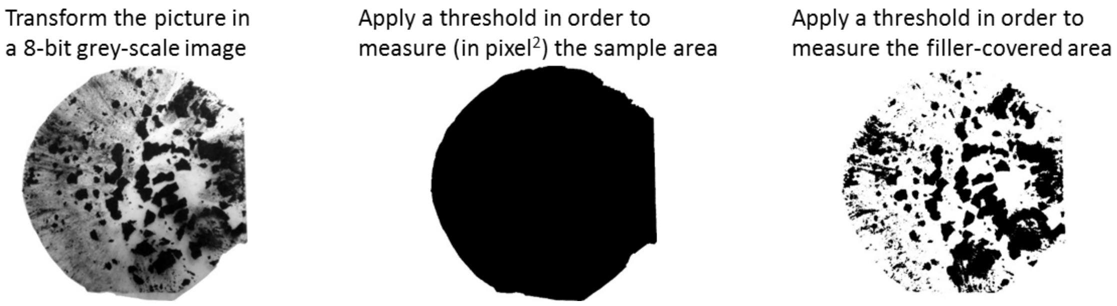

Transform the picture in a 8-bit grey-scale image

Apply a threshold in order to measure (in pixel^2) the sample area

Apply a threshold in order to measure the filler-covered area

Figure S11. Method used to calculate the area of a sample, and its fraction covered by nanofiller.

With this method, we calculated a distribution-rate of (3.5 ± 2.0)·10^{-3} for GNP in LLDPE, by analysing the pictures taken during the first four P&F cycles. Despite this method may not be accurate, it still gives a good estimation of the distribution-rate. Indeed, the distribution-rate found from the fitting of the mechanical and electrical properties resulted quite similar, and equal to (3.3 ± 1.4)·10^{-3} (see Section S.10.3).

As the distribution-rate is important for the determination of the dispersion level of a nanofiller, in Table S5 we reported the distribution rates of different nanofiller/matrix systems.

Table S5. ***Distribution-rates for different nanofiller/matrix systems***.

Matrix / Filler	LLDPE	HDPE	Phenoxy	PC	TPU
C-Therm 002 S = 25 m^2/g	$(3.5 \pm 2.0)\cdot 10^{-3}$	$(9.3 \pm 1.5)\cdot 10^{-3}$	$(7.4 \pm 1.0)\cdot 10^{-3}$	$(2.3 \pm 1.0)\cdot 10^{-3}$	$(5.43 \pm 0.23)\cdot 10^{-3}$
xGnP 750 S = 100 m^2/g *	$(2.6 \pm 0.4)\cdot 10^{-3}$	$(2.58 \pm 0.11)\cdot 10^{-3}$	$(3.9 \pm 1.7)\cdot 10^{-3}$	$(1.6 \pm 0.3)\cdot 10^{-3}$	$(1.63 \pm 0.14)\cdot 10^{-3}$
MMT (Cloisite 20A) S ≈ 800 m^2/g	$\geq 7\cdot 10^{-2}$	$\geq 10\cdot 10^{-2}$	$\geq 2\cdot 10^{-2}$		$\geq 3\cdot 10^{-2}$

* *S* calculated from XRD thickness: $S \approx 2/(d \cdot t_{XRD})$, where *d* is the density of graphite

Note that for the case of montmorillonite (MMT) nanocomposites, the MMT agglomerates disappear during the dispersion process, leaving the samples transparent. Therefore, we recorded the number *n* of P&F cycles needed to obtain a sample transparent to the naked eye and free of white agglomerates. We believe that when a sample does not show MMT agglomerates anymore, then the dispersion-factor must be at least 50%. Therefore, we estimated the distribution-rate with the following equation:

$$I = \frac{1}{n} ln\left(\frac{A_p - A_0}{0.5A_p}\right)$$

Equation S24.

The distribution-rates of MMT results to be much higher than GNP powders, and this might be due to the functionalization of the MMT used, or to a better nanofiller/matrix interaction that aid the dispersion process.

We tried to disperse also immiscible materials like magnetite nanoparticles and LLDPE, and we found that they can be well-mixed with a number of cycles higher than 200 (see figure below).

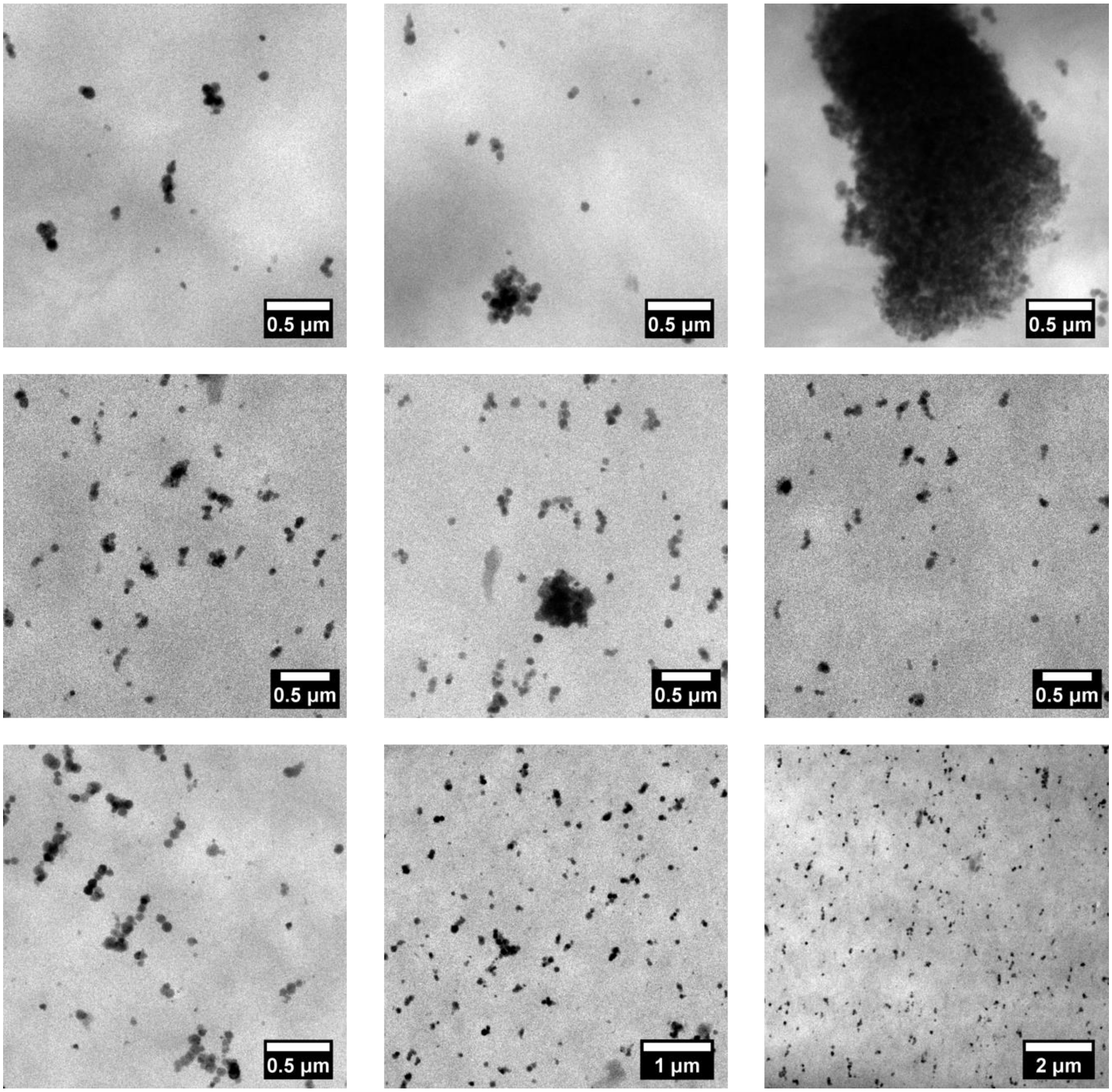

Figure S12. TEM images of LLDPE nanocomposites with 1.72 wt.% magnetite nanoparticles.

S.12 Potential applications

S.12.1 Joule-heating

Self-heating of nanocomposites was due to Joule effect when different electrical potentials were applied to the extremities of the samples (Figure S13). The inset pictures of the samples (Figure S13a, b, and c) were taken with a thermal camera, and show good thermal homogeneity reflecting an optimal microstructure. Note how the sample containing 7.4 vol.% GNP with a dispersion level of 48.2% (Figure S13b) heated up less than the sample containing 4.8 vol.% GNP (Figure S13a) because it's nanofiller dispersion state was grater, so less conductive paths were available for Joule heating.

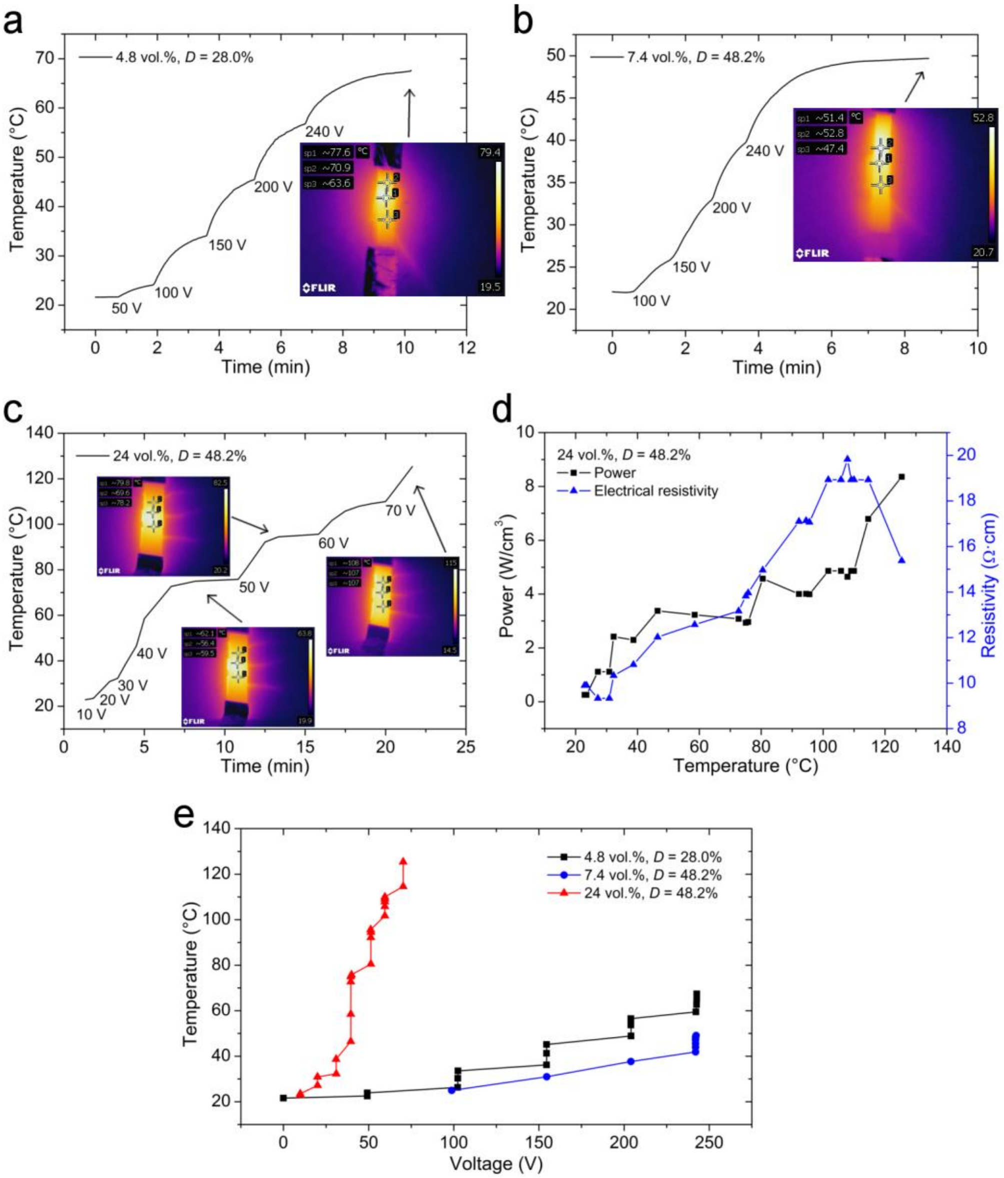

*Figure S13. Self-heating tests of LLDPE nanocomposites with different GNP loadings and dispersion levels. (**a**) Sample containing 4.8 vol.% GNP with a dispersion level of 28% reached a temperature of ~70 °C when 240 V of AC electrical potential difference was applied to its extremities. (**b**) Sample containing 7.4 vol.% GNP with a dispersion level of 48.2% reached only a temperature of ~50 °C after 240 V were applied. (**c**) Sample containing 24 vol.% GNP with a dispersion level of 48.2% reached the melting point after 70 V were applied; the power supplied to this sample and its resistivity increased with temperature (**d**). (**e**) Comparison of the self-heating behaviour of the tested samples as a function of the applied AC electrical potential difference.*

S.12.2 Strain sensing

Strain sensing during tensioning of nanocomposites (Figure S14) reveals that the variation of electrical resistance is much more evident for samples containing lower amounts of GNP. The sample containing 4.8 vol.% GNP with a dispersion level of 28% (close to the critical dispersion level D_c) presents a resistance variation similar to the sample of same composition but higher dispersion level (48.2%) only at high strains, when its conductivity approaches the theoretical one, σ_{th}. All nanocomposites presented several orders of magnitude variation in resistance before yielding (which occured around 15% of strain), demonstrating their suitability for structural health monitoring applications.

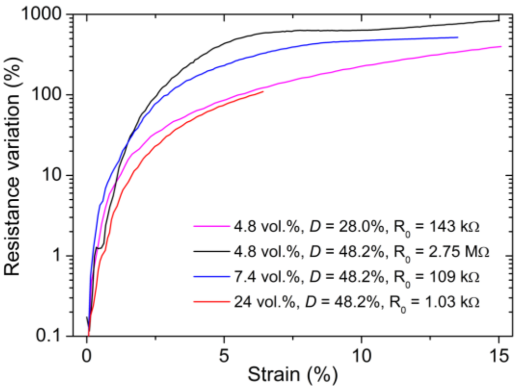

Figure S14. Variation of electrical resistance of LLDPE nanocomposites containing different GNP loadings and GNP dispersion states as a function of tensile strain.

S.12.3 Energy management

Polymer nanocomposites could be employed as high dielectric constant (high-k) and low loss materials for gate dielectrics, energy storage devices or electroactive materials.[29] Nanocarbon-polymer composites satisfy the synergistic requirements of high-k and limited loss just before reaching the percolation threshold. Above this point there is a huge increase in the dielectric loss, due to the ohmic electrical conduction of the percolated network. Figure 4a of the main paper shows how nanofiller agglomeration (samples containing 4.8 vol.% GNP with dispersion levels of 28% and 48.2%) reflects in conductive nanocomposites that are mainly resistive: the imaginary (Z'') *vs.* real impedance (Z') Nyquist plots of these samples show very small values of Z'' for a constant value of Z' (diverging slightly only at high frequencies due to the contact resistance). Higher dispersion levels and distribution of aligned GNP inside the dielectric LLDPE matrix result in nanocomposites with a capacitive behaviour (sample containing 4.8 vol.% GNP with a dispersion level 80.6%, see the $C_3 || R_3$ equivalent circuit, shown also in Figure S15b). This can be useful for high-k applications as they exhibit a high dielectric constant combined with a low dielectric loss.

Figure S15 shows the admittance magnitude of LLDPE nanocomposites containing 4.8 vol.% GNP with different nanofiller dispersion states. Admittance (Y), which is inversely proportional to impedance,[30] has been plotted to facilitate the relationship of AC-properties with DC-conductivity measurements. First, the pristine polymer that initially exhibits a purely capacitive behaviour (linear frequency-dependence, Figure S15a) is transformed into a conductive material (non-frequency dependant) when containing agglomerated states (*D*-factor of 28% and 48.2%) of 4.8 vol.% GNP. The different trends of |Y| along frequency support our previous observations of the electrical conductivity as a function of nanofiller dispersion (shown in Figure 2d of the main text), hence in accordance with the behaviour expected by Equation S16. Indeed, a slight agglomeration of nanofiller allows a conductive percolation network inside the material (admittance is predominantly real, Ohmic conduction), especially when is close to the critical dispersion level, D_c, of Equation S16 (which corresponds to 25% for our nanocomposites containing 4.8 vol.% GNP). In such case, nanocomposites might be represented by the resistive equivalent circuit shown in Figure S15b (R_1 and R_2). However, when the nanofiller dispersion is increased, the nanocomposite conductivity decreases from high values (the highest is σ_M at the critical dispersion level) to lower values (approaching the theoretical conductivity, σ_{th}, expected by Equation S16 at high nanofiller dispersion states), because the percolation network becomes "disconnected" in many points. These "dead-ends" contribute to the formation of micro-capacitors at those conductive/dielectric/conductive regions of well-dispersed platelets with non-negligible interparticle gaps. Nanocomposites with such a microstructure containing highly dispersed GNP can be represented by a parallel R-C equivalent circuit, as depicted in Figure S15b (R_3 and C_3), and a frequency-dependent admittance is observed (see sample with *D*-factor = 80.6% in Figure S15a). Contrary to the common believe, this absence of percolation in nanocarbon/polymer nanocomposites can be also exploited for technological applications where dielectric materials with a high dielectric constant (real permittivity, ε') and a low dielectric loss (imaginary permittivity, ε'') are needed (*e.g.* gate dielectrics, energy storage devices, electroactive materials).[29] The real component of permittivity for dielectric/conductor nanocomposites is a measure of the migration and accumulation of charges at the dielectric/conductor interfaces (Maxwell–Wagner–Sillars polarization)[31], while the imaginary part is related to dielectric and conduction losses, associated to the material's ohmic resistance and the induced polarization, respectively. As seen from Figure S15c, the imaginary permittivity of the resistive samples (*D*-factors of 28% and 48.2%) is as high as 10^8 at low frequencies and decreases to 10^2 at 1 MHz. The sample with a high nanofiller dispersion of 80.6% has an imaginary permittivity that remains notably low, between 100 and 0.1 throughout the entire frequency window. Furthermore, this last sample shows a loss tangent ($\varepsilon''/\varepsilon'$) as low as ~0.1 (Figure S15d), in comparison with values above 10 for samples with lower nanofiller dispersions (*D*-factors of 28% and 48.2%). These results confirm that the electrical properties of GNP-polymer nanocomposites can be tailored by the nanofiller dispersion state, exploiting the needs of a wide variety of conductive or insulating (capacitive) applications.

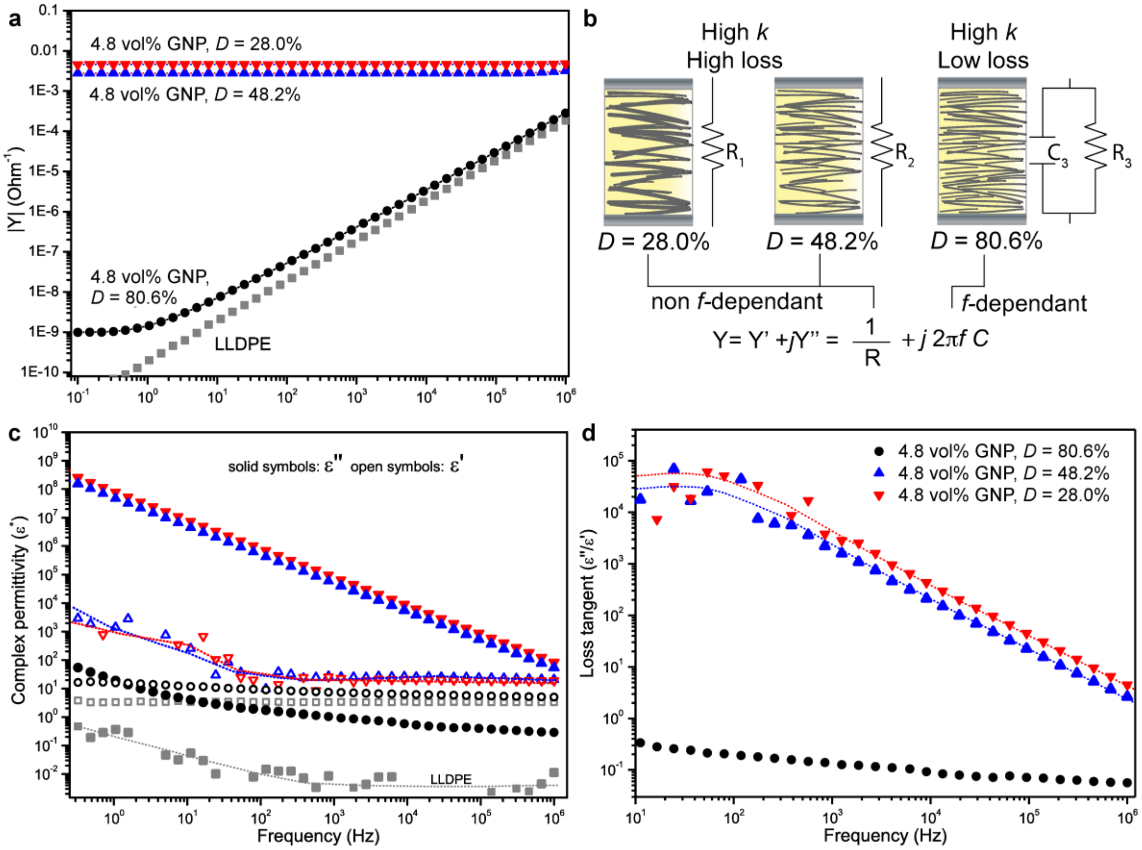

*Figure S15. Frequency sweep of: (**a**) admittance modulus (|Y|), (**c**) complex permittivity, and (**d**) loss tangent for LLDPE nanocomposites containing 4.8 vol.% GNP with different nanofiller dispersion levels. (**b**) Draw that summarizes the observed behaviours: while a nanofiller dispersion close to the critical dispersion level, D_c (≈ 25% for these samples), of Equation S16 makes the nanocomposites conductive (resistive, R_1 and R_2), high dielectric constant (ε', high-k) and low loss tangent ($\varepsilon''/\varepsilon'$) nanocomposites can be addressed only if the nanofiller dispersion state is optimized (close to 100%).*

S.12.4 MMT nanocomposites

Nanocomposites of LLDPE and montmorillonite were prepared introducing a high amount of Cloisite 20A between two polymeric films. The sample was characterised after 50 P&F cycles, because at this number of cycles should correspond a MMT dispersion of ~99% considering the distribution-rate found in Section S.10.4. Thermal gravimetric analysis (TGA) revealed a MMT content of ~74 wt.%. Tensile tests revealed a Young’s modulus of ~1.8 GPa, a strength of ~12.5 MPa, and a strain at break of ~1%.

We also prepared a reference sample with a mini-extruder. We managed to introduce ~50 wt.% MMT in several steps, differently from the P&F sample in which LLDPE and MMT were mixed in one-go. TGA revealed a final MMT content of ~48 wt.%. The lower concentration of MMT of this sample compared to the P&F one reflected on higher strain at break (~12%), but lower stiffness (~320 MPa) and strength (~9.3 MPa).

In order to assess our nanocomposites, Table S6 reports the mechanical reinforcement found in literature for MMT nanocomposites with non-elastomeric matrices. Our P&F sample is the highest loaded and reinforced sample ever reported for nanocomposites prepared by melt-blending. Our other sample prepared with the mini-extruder has a mechanical reinforcement similar to those found in literature for melt-blended nanocomposites. Only bottom-up techniques, such as solution processing and layer-by-layer, can reach the same loading and mechanical reinforcement of our P&F sample. The box chart of Figure 4d in the main text is based on the data of Table S6.

Table S6. ***Mechanical reinforcement found in literature for MMT nanocomposites prepared by melt processing, solution processing, or layer-by-layer***.

Processing technique	Matrix	MMT content (wt.%)	Mechanical reinforcement (E_c/E_m)	Reference
Melt blending	PVC	0.5	1.01	32
		1	1.01	
		3	1.06	
		5	1.04	
Solution processing	PLA	2	1.22	33
		4	1.36	
		6	1.33	
		8	1.31	
Melt blending	PA6	1.5	1.26	34
		2.9	1.53	
		4.6	1.69	
		6.6	1.85	
Melt blending	PA6	2	1.30	34
		4	1.50	
		6.5	1.73	
Solution processing	PET	1	1.30	35
		2	1.49	
		3	1.85	
Solution processing	PVA	2	1.80	36
		4	3.10	
		6	2.75	
		10	3.40	
Solution processing	PS	3.6	1.15	37
		5.6	1.31	
		7.6	1.59	
Melt blending	PBS	1.5	1.19	38
		2.5	1.42	
		4	1.80	
		5.5	3.46	
Melt blending	LLDPE	0.8	1.39	39
		2.5	1.80	
		4.6	2.52	
		6.9	2.99	
Melt blending	PLA	1.2	1.46	40
		3	1.49	
		4	1.65	
Solution processing	PS	5	1.07	41
		10	1.57	
		20	2.18	
		30	1.51	

Solution processing	Chitosan	2.5	1.09	42
		5	1.16	
		10	1.26	
Solution processing	Polyester	3	1.12	43
		5	1.22	
		7	1.18	
		10	1.32	
Melt blending	PLA	2.5	1.17	44
		5	1.32	
		7.5	1.50	
Solution processing	PLA	2	1.22	45
		4	1.37	
		6	1.32	
		8	1.31	
Solution processing	PLA	2	1.21	45
		4	1.29	
		6	1.49	
		8	3.04	
Melt blending	LDPE	3	1.02	46
		6	1.03	
Melt blending	PA6	2.7	1.45	47
		4.9	1.66	
Solution processing	Cellulose	1	1.01	48
		5	1.56	
		10	1.55	
		25	1.69	
		50	1.67	
Solution processing	PEO	76	6.25	49
		85	15.9	
Solution processing	Cellulose	60	3.70	49
		83	5.80	
LbL	PVA	70	7.64	50
LbL	PVA-GA	70	53.0	50
LbL	PDDA	80	68.7	51
LbL	Chitosan	80	3.21	52
LbL	PVA	70	7.64	53
		70	24.1	
		70	34.1	
LbL	PAA	70	6.14	54
LbL	PVA	55	5.89	55
LbL	PVA	96	2.22	56
		97	4.88	
		98	24.8	
		99	18.8	
LbL	PVP	95	3.80	57

S.13 Classical composite theories

S.13.1 Halpin-Tsai model

The mechanical reinforcement due to a nanofiller – which can be defined as the ratio between the Young's moduli of the nanocomposite (E_c) and the neat polymer (E_m) – depends on its aspect-ratio ξ (the ratio between its diameter and thickness, assuming a disc-like platelet), volume fraction V_p, and Young's modulus of the filler (E_p). Therefore, assuming an in-plane nanofiller orientation, it is possible to predict the mechanical reinforcement along the plane of a nanocomposite by using the Halpin-Tsai equations:[58,59]

$$\frac{E_c}{E_m} = \frac{1 + \zeta \eta V_p}{1 - \eta V_p}$$

Equation S25.

with

$$\eta = \frac{\frac{E_p}{E_m} - 1}{\frac{E_p}{E_m} + \zeta}$$

Equation S26.

where ζ is a shape-factor, which depends on the nanofiller aspect-ratio:[60]

$$\zeta = \frac{2}{3}\xi$$

Equation S27.

Note that if $\xi \rightarrow \infty$, the Halpin-Tsai model equals the (upper bound) rule of mixtures (RoM), whereas if $\xi \rightarrow 0$, it equals the (lower bound) inverse rule of mixtures (IRoM).

S.13.2 Pukanszky model

The size of a nanofiller is connected to its specific surface area, which can influence the yield stress Y_c of a nanocomposite. This is taken into account by the interaction parameter B_{Puk} of the Pukanszky model:[61]

$$Y_c = Y_m \frac{1 - V_p}{1 + 2.5V_p} e^{B_{Puk} \cdot V_p}$$

Equation S28.

where Y_m is the yield stress of the polymer matrix. Moreover, the stronger the interaction between nanofiller and matrix, the higher the parameter B_{Puk}, resulting in higher yield stress values.

S.14 References

(1) Kuila, T.; Bose, S.; Mishra, A. K.; Khanra, P.; Kim, N. H.; Lee, J. H. Effect of Functionalized Graphene on the Physical Properties of Linear Low Density Polyethylene Nanocomposites. *Polym. Test.* **2012**, *31*, 31–38

(2) Kundu, P. P.; Biswas, J.; Kim, H.; Choe, S. Influence of Film Preparation Procedures on the Crystallinity, Morphology and Mechanical Properties of LLDPE Films. *Eur. Polym. J.* **2003**, *39*, 1585–1593

(3) Hermans, P. H.; Weidinger, A. On the Determination of the Crystalline Fraction of Polyethylenes from X-Ray Diffraction. *Makromol. Chem.* **1961**, *44*, 24–36

(4) Oskouyi, A. B.; Sundararaj, U.; Mertiny, P. Current-Voltage Characteristics of Nanoplatelet-Based Conductive Nanocomposites. *Nanoscale Res. Lett.* **2014**, *9*, 1–8

(5) Nezakati, T.; Tan, A.; Seifalian, A. M. Enhancing the Electrical Conductivity of a Hybrid POSS–PCL/Graphene Nanocomposite Polymer. *J. Colloid Interface Sci.* **2014**, *435*, 145–155

(6) Kouroupis-Agalou, K.; Liscio, A.; Treossi, E.; Ortolani, L.; Morandi, V.; Pugno, N. M.; Palermo, V. Fragmentation and Exfoliation of 2-Dimensional Materials: A Statistical Approach. *Nanoscale* **2014**, *6*, 5926

(7) Krzesińska, M.; Celzard, A.; Marêché, J. F.; Puricelli, S. Elastic Properties of Anisotropic Monolithic Samples of Compressed Expanded Graphite Studied with Ultrasounds. *J. Mater. Res.* **2001**, *16*, 606–614

(8) Sun, G.; Li, X.; Qu, Y.; Wang, X.; Yan, H.; Zhang, Y. Preparation and Characterization of Graphite Nanosheets from Detonation Technique. *Mater. Lett.* **2008**, *62*, 703–706

(9) Howe, J. Y.; Cavin, B. O.; Drakeford, A. E.; Peascoe, R. A.; Zontek, T. L.; Miller, D. J. Influence of Bulk Graphite Thickness on the Accuracy of X-Ray Diffraction Measurement. In *Carbon 2007*; Seattle, Washington, USA, 2007

(10) Chung, D. D. L. Review Graphite. *J. Mater. Sci.* **2002**, *37*, 1475–1489

(11) Blanton, T. N.; Majumdar, D. X-Ray Diffraction Characterization of Polymer Intercalated Graphite Oxide. *Powder Diffr.* **2012**, *27*, 104–107

(12) Gong, L.; Young, R. J.; Kinloch, I. A.; Riaz, I.; Jalil, R.; Novoselov, K. S. Optimizing the Reinforcement of Polymer-Based Nanocomposites by Graphene. *ACS Nano* **2012**, *6*, 2086–2095

(13) Chen, W.; Qu, B. LLDPE/ZnAl LDH-Exfoliated Nanocomposites: Effects of Nanolayers on Thermal and Mechanical Properties. *J. Mater. Chem.* **2004**, *14*, 1705

(14) Wirsén, A.; Lindberg, K. T.; Albertsson, A.-C. Graft Polymerization of Acrylamide onto Linear Low-Density Polyethylene Film by Electron Beam Pre-Irradiation in Air or Argon: 3. Morphology. *Polymer* **1996**, *37*, 761–769

(15) Zhang, K.; Zhang, Y.; Wang, S. Enhancing Thermoelectric Properties of Organic Composites through Hierarchical Nanostructures. *Sci. Rep.* **2013**, *3*

(16) Seung Hun, H.; Hae-Mi, J.; Sung-Ho, C. X-Ray Diffraction Patterns of Thermally-Reduced Graphenes. *J. Korean Phys. Soc.* **2010**, *57*, 1649

(17) Vasileiou, A. A.; Kontopoulou, M.; Docoslis, A. A Noncovalent Compatibilization Approach to Improve the Filler Dispersion and Properties of Polyethylene/Graphene Composites. *ACS Appl. Mater. Interfaces* **2014**, *6*, 1916–1925

(18) Kim, H.; Kobayashi, S.; AbdurRahim, M. A.; Zhang, M. J.; Khusainova, A.; Hillmyer, M. A.; Abdala, A. A.; Macosko, C. W. Graphene/Polyethylene Nanocomposites: Effect of Polyethylene Functionalization and Blending Methods. *Polymer* **2011**, *52*, 1837–1846

(19) Carotenuto, G.; De Nicola, S.; Palomba, M.; Pullini, D.; Horsewell, A.; Hansen, T. W.; Nicolais, L. Mechanical Properties of Low-Density Polyethylene Filled by Graphite Nanoplatelets. *Nanotechnology* **2012**, *23*, 485705

(20) Constantin, D. Linear-low-density Polyethylene Melt Rheology: Extensibility and Extrusion Defects. *Polym. Eng. Sci.* **1984**, *24*, 268–274

(21) Dartora, P. C.; Santana, R. M. C.; Moreira, A. C. F.; Dartora, P. C.; Santana, R. M. C.; Moreira, A. C. F. The Influence of Long Chain Branches of LLDPE on Processability and Physical Properties. *Polímeros* **2015**, *25*, 531–539

(22) Mackley, M. R.; Spitteler, P. H. J. Experimental Observations on the Pressure-Dependent Polymer Melt Rheology of Linear Low Density Polyethylene, Using a Multi-Pass Rheometer. *Rheol. Acta* **1996**, *35*, 202–209

(23) Liang, J. Z.; Ness, J. N. Studies on Melt Flow Properties of Low Density and Linear Low Density Polyethylene Blends in Capillary Extrusion. *Polym. Test.* **1997**, *16*, 173–184

(24) Steffl, T. Rheological and Film Blowing Properties of Various Low Density Polyethylenes and Their Blends, Erlangen-Nürnberg, Univ., Diss., 2004

(25) Leider, P. J.; Bird, R. B. Squeezing Flow between Parallel Disks. I. Theoretical Analysis. *Ind. Eng. Chem. Fundam.* **1974**, *13*, 336–341

(26) Engmann, J.; Servais, C.; Burbidge, A. S. Squeeze Flow Theory and Applications to Rheometry: A Review. *J. Non-Newton. Fluid Mech.* **2005**, *132*, 1–27

(27) Barwich, S.; Coleman, J. N.; Möbius, M. E. Yielding and Flow of Highly Concentrated, Few-Layer Graphene Suspensions. *Soft Matter* **2015**, *11*, 3159–3164

(28) Li, J.; Kim, J.-K. Percolation Threshold of Conducting Polymer Composites Containing 3D Randomly Distributed Graphite Nanoplatelets. *Compos. Sci. Technol.* **2007**, *67*, 2114–2120

(29) Yuan, J.; Luna, A.; Neri, W.; Zakri, C.; Schilling, T.; Colin, A.; Poulin, P. Graphene Liquid Crystal Retarded Percolation for New High-k Materials. *Nat. Commun.* **2015**, *6*, 8700

(30) Sandler, J.; Shaffer, M. S. P.; Prasse, T.; Bauhofer, W.; Schulte, K.; Windle, A. H. Development of a Dispersion Process for Carbon Nanotubes in an Epoxy Matrix and the Resulting Electrical Properties. *Polymer* **1999**, *40*, 5967–5971

(31) Dang, Z.-M.; Yuan, J.-K.; Yao, S.-H.; Liao, R.-J. Flexible Nanodielectric Materials with High Permittivity for Power Energy Storage. *Adv. Mater.* **2013**, *25*, 6334–6365

(32) Wan, C.; Qiao, X.; Zhang, Y.; Zhang, Y. Effect of Different Clay Treatment on Morphology and Mechanical Properties of PVC-Clay Nanocomposites. *Polym. Test.* **2003**, *22*, 453–461

(33) Chang, J.-H.; An, Y. U.; Sur, G. S. Poly(Lactic Acid) Nanocomposites with Various Organoclays. I. Thermomechanical Properties, Morphology, and Gas Permeability. *J. Polym. Sci. Part B Polym. Phys.* **2003**, *41*, 94–103

(34) Shah, R. K.; Paul, D. R. Nylon 6 Nanocomposites Prepared by a Melt Mixing Masterbatch Process. *Polymer* **2004**, *45*, 2991–3000

(35) Chang, J.-H.; Kim, S. J.; Joo, Y. L.; Im, S. Poly(Ethylene Terephthalate) Nanocomposites by in Situ Interlayer Polymerization: The Thermo-Mechanical Properties and Morphology of the Hybrid Fibers. *Polymer* **2004**, *45*, 919–926

(36) Strawhecker, K. E.; Manias, E. Structure and Properties of Poly(Vinyl Alcohol)/Na^{+} Montmorillonite Nanocomposites. *Chem. Mater.* **2000**, *12*, 2943–2949

(37) Fu, X.; Qutubuddin, S. Polymer–Clay Nanocomposites: Exfoliation of Organophilic Montmorillonite Nanolayers in Polystyrene. *Polymer* **2001**, *42*, 807–813

(38) Sinha Ray, S.; Okamoto, K.; Okamoto, M. Structure−Property Relationship in Biodegradable Poly(Butylene Succinate)/Layered Silicate Nanocomposites. *Macromolecules* **2003**, *36*, 2355–2367

(39) Hotta, S.; Paul, D. R. Nanocomposites Formed from Linear Low Density Polyethylene and Organoclays. *Polymer* **2004**, *45*, 7639–7654

(40) Maiti, P.; Yamada, K.; Okamoto, M.; Ueda, K.; Okamoto, K. New Polylactide/Layered Silicate Nanocomposites: Role of Organoclays. *Chem. Mater.* **2002**, *14*, 4654–4661

(41) Noh, M. W.; Lee, D. C. Synthesis and Characterization of PS-Clay Nanocomposite by Emulsion Polymerization. *Polym. Bull.* **1999**, *42*, 619–626

(42) Wang, S. F.; Shen, L.; Tong, Y. J.; Chen, L.; Phang, I. Y.; Lim, P. Q.; Liu, T. X. Biopolymer Chitosan/Montmorillonite Nanocomposites: Preparation and Characterization. *Polym. Degrad. Stab.* **2005**, *90*, 123–131

(43) Kornmann, X.; Berglund, L. A.; Sterte, J.; Giannelis, E. P. Nanocomposites Based on Montmorillonite and Unsaturated Polyester. *Polym. Eng. Sci.* **1998**, *38*, 1351–1358

(44) Jiang, L.; Zhang, J.; Wolcott, M. P. Comparison of Polylactide/Nano-Sized Calcium Carbonate and Polylactide/Montmorillonite Composites: Reinforcing Effects and Toughening Mechanisms. *Polymer* **2007**, *48*, 7632–7644

(45) Chang, J.-H.; An, Y. U.; Cho, D.; Giannelis, E. P. Poly(Lactic Acid) Nanocomposites: Comparison of Their Properties with Montmorillonite and Synthetic Mica (II). *Polymer* **2003**, *44*, 3715–3720

(46) Morawiec, J.; Pawlak, A.; Slouf, M.; Galeski, A.; Piorkowska, E.; Krasnikowa, N. Preparation and Properties of Compatibilized LDPE/Organo-Modified Montmorillonite Nanocomposites. *Eur. Polym. J.* **2005**, *41*, 1115–1122

(47) Chavarria, F.; Paul, D. R. Comparison of Nanocomposites Based on Nylon 6 and Nylon 66. *Polymer* **2004**, *45*, 8501–8515

(48) Wu, C.-N.; Saito, T.; Fujisawa, S.; Fukuzumi, H.; Isogai, A. Ultrastrong and High Gas-Barrier Nanocellulose/Clay-Layered Composites. *Biomacromolecules* **2012**, *13*, 1927–1932

(49) Sehaqui, H.; Kochumalayil, J.; Liu, A.; Zimmermann, T.; Berglund, L. A. Multifunctional Nanoclay Hybrids of High Toughness, Thermal, and Barrier Performances. *ACS Appl. Mater. Interfaces* **2013**, *5*, 7613–7620

(50) Podsiadlo, P.; Kaushik, A. K.; Arruda, E. M.; Waas, A. M.; Shim, B. S.; Xu, J.; Nandivada, H.; Pumplin, B. G.; Lahann, J.; Ramamoorthy, A.; Kotov, N. A. Ultrastrong and Stiff Layered Polymer Nanocomposites. *Science* **2007**, *318*, 80–83

(51) Tang, Z.; Kotov, N. A.; Magonov, S.; Ozturk, B. Nanostructured Artificial Nacre. *Nat. Mater.* **2003**, *2*, 413–418

(52) Podsiadlo, P.; Tang, Z.; Shim, B. S.; Kotov, N. A. Counterintuitive Effect of Molecular Strength and Role of Molecular Rigidity on Mechanical Properties of Layer-by-Layer Assembled Nanocomposites. *Nano Lett.* **2007**, *7*, 1224–1231

(53) Podsiadlo, P.; Kaushik, A. K.; Shim, B. S.; Agarwal, A.; Tang, Z.; Waas, A. M.; Arruda, E. M.; Kotov, N. A. Can Nature's Design Be Improved Upon? High Strength, Transparent Nacre-Like Nanocomposites with Double Network of Sacrificial Cross Links †. *J. Phys. Chem. B* **2008**, *112*, 14359–14363

(54) Huang, G.; Ge, C.; He, B. Preparation, Characterization and Properties of Amino-Functionalized Montmorillonite and Composite Layer-by-Layer Assembly with Inorganic Nanosheets. *Appl. Surf. Sci.* **2011**, *257*, 7123–7128

(55) Gaidukov, S.; Danilenko, I.; Gaidukova, G. Characterization of Strong and Crystalline Polyvinyl Alcohol/Montmorillonite Films Prepared by Layer-by-Layer Deposition Method. *Int. J. Polym. Sci.* **2015**, *2015*, 1–8

(56) Shu, Y.; Yin, P.; Liang, B.; Wang, H.; Guo, L. Bioinspired Design and Assembly of Layered Double Hydroxide/Poly(Vinyl Alcohol) Film with High Mechanical Performance. *ACS Appl. Mater. Interfaces* **2014**, 140825162306007

(57) Finnemore, A.; Cunha, P.; Shean, T.; Vignolini, S.; Guldin, S.; Oyen, M.; Steiner, U. Biomimetic Layer-by-Layer Assembly of Artificial Nacre. *Nat. Commun.* **2012**, *3*, 966

(58) Affdl, J. C. H.; Kardos, J. L. The Halpin-Tsai Equations: A Review. *Polym. Eng. Sci.* **1976**, *16*, 344–352

(59) Halpin, J. C.; Thomas, R. L. Ribbon Reinforcement of Composites. *J. Compos. Mater.* **1968**, *2*, 488–497

(60) Van Es, M. A.; Van Turnhout, J. Polymer-Clay Nanocomposites: The Importance of Particle Dimensions. Ph.D. Thesis, Delft University of Technology, 2001

(61) Turcsányi, B.; Pukánszky, B.; Tüdõs, F. Composition Dependence of Tensile Yield Stress in Filled Polymers. *J. Mater. Sci. Lett.* **1988**, *7*, 160–162